

## Earth-based observations of radar-dark crater haloes on the Moon: Implications for regolith properties

Rebecca R. Ghent, David W. Leverington, and Bruce A. Campbell

Center for Earth and Planetary Studies, Smithsonian Institution, Washington, D. C., USA

B. Ray Hawke

Hawaii Institute of Geophysics and Planetology, School of Ocean and Earth Science and Technology, Honolulu, Hawaii, USA

Donald B. Campbell

Department of Astronomy, Cornell University, Ithaca, New York, USA

Received 28 September 2004; revised 16 November 2004; accepted 14 December 2004; published 16 February 2005.

[1] Earth-based radar can be used in conjunction with other data sets collected remotely or in situ to characterize the physical and chemical properties of the lunar regolith. We use previously existing and newly acquired Earth-based radar measurements at 70-cm wavelength to investigate the properties of distinctive low-return haloes surrounding 39 nearside impact craters. These haloes are distinct from the well-known optically dark haloes associated with volcanic craters or with impacts into cryptomare deposits. We examine two possible mechanisms for formation of radar-dark haloes: (1) excavation of high-TiO<sub>2</sub>, high-loss tangent basalt and (2) deposition of a mantling layer produced in the impact process that is depleted in meter-sized blocks. Comparison of the radar data with Apollo and Lunar Orbiter images indicates a general spatial correspondence between radar-dark crater haloes and radial ridged ejecta facies distal to the radar-bright crater rims. Comparison with Clementine UV/VIS multispectral data indicates no apparent spatial correlation between regions of enhanced TiO<sub>2</sub> content and radar-dark haloes; though variations in TiO<sub>2</sub> content may play a role for some mare craters, they are insufficient to account for the observed offsets in radar echo power. We conclude that the radar-dark haloes result from a block-poor ejecta deposit that disappears over time with meteoroid bombardment. A more detailed and comprehensive analysis of ejecta degradation processes and rates following acquisition of additional high-resolution radar data could lead to a refinement of the lunar geologic timescale.

**Citation:** Ghent, R. R., D. W. Leverington, B. A. Campbell, B. R. Hawke, and D. B. Campbell (2005), Earth-based observations of radar-dark crater haloes on the Moon: Implications for regolith properties, *J. Geophys. Res.*, *110*, E02005, doi:10.1029/2004JE002366.

### 1. Introduction

[2] Earth-based radar has been used for over 30 years to image the nearside of the Moon and to investigate the physical properties of the lunar regolith [e.g., *Thompson et al.*, 1970; *Thompson*, 1974; *Schaber et al.*, 1975; *Stacy*, 1993; *Campbell et al.*, 1997]. The physical characteristics of the regolith are of importance to significant questions in lunar geology, such as understanding the spatial limits and relative timing of flow units or of materials associated with impacts. In contrast with spectral reflectance methods that are sensitive to chemical variations in the upper several microns of surface materials, radar signals penetrate to greater depths and thus return information representing a larger integrated volume of regolith. Improved resolution in

both Earth-based radar and orbital multispectral data provide a new opportunity to explore the physical and chemical properties of the lunar regolith at a variety of scales. In this work, we focus on distinctive radar-dark haloes surrounding nearside impact craters. These haloes show characteristically low radar returns in Earth-based observations at 70-cm wavelength and have not been examined systematically to date, though they were noted in previous work [e.g., *Thompson et al.*, 1970; *Thompson*, 1974; *Schultz and Mendell*, 1978]. Using previously existing and newly acquired Earth-based radar observations at 70-cm wavelength in conjunction with UV/VIS multispectral data from the Clementine mission, we investigate variations in physical and/or chemical properties that may be responsible for the presence of radar-dark haloes. In addition, we are interested in understanding the implications of radar-dark haloes for impact-related processes, the longevity of the haloes in the face of ongoing bombardment by impactors of various

**Table 1.** Nearside Craters With Radar-Dark Haloes

Crater	Lat., °N	Lon., °E	D, km	Setting <sup>a</sup>	Age (Reference) <sup>b</sup>	Radar-Bright Ejecta Width <sup>c</sup> ( $r_c$ )	Radar-Dark Halo Width <sup>d</sup> ( $r_c$ )
Angström	29.9	-41.6	9	M	E (1)	≤1.0	≤4.0
Aristarchus <sup>c</sup>	23.7	-47.4	40	HM	C	1.0	1.5
Aristoteles <sup>c</sup>	50.2	17.4	87	HM	E	≤1.0	1.5
Atlas	46.7	44.4	87	H	LI	0.5	2.0
Autolycus	30.7	1.5	39	M	C	≤1.5	≤2.0
Bessel	21.8	17.9	15	M	E (2)	—	1–2
Bullialdus <sup>c</sup>	-20.7	-22.2	60	M	E	≤1.0	1.0
Byrgius D	-24.2	-67.5	28	H	LI (3)	—	≤2.0
Cardanus	13.2	-72.5	49	HM	LI	1.0	≤4.0
Cepheus	40.8	45.8	39	H	E	≤1.0	≤2.0
Copernicus	9.7	-20.1	93	HM	C	≤1.0	≤1.0
Delisle	29.9	-34.6	25	M	E	≤1.0	≤4.0
Diophantus	27.6	-34.3	17	M	E	≤1.0	≤1.5
Eichstadt	-22.6	-78.3	49	H	E (4)	≤1.0	≤2.0
Euler	23.3	-29.2	27	M	E	≤1.3	≤3.0
Franklin	38.8	47.7	56	H	LI	≤1.0	≤2.0
Galle	55.9	22.3	21	M	E (5)	≤1.0	1.0
Galilaei <sup>c</sup>	10.5	-62.7	15	M	E (6)	—	≤3.0
Galilaei A <sup>c</sup>	11.7	-62.9	11	M	E (6)	—	≤3.0
Hainzel A <sup>f</sup>	-40.5	-33.5	55	H	E (7)	≤0.5	≤1.5
Hausen	-65.0	-88.1	167	H	E (8)	0.5	≤2.0
Hercules	46.7	39.1	69	HM	E	0.5	2.0
Herodotus A	21.5	52.0	9	M	E (9)	≤0.5	≤3.0
Krafft	16.6	-72.6	51	HM	LI	1.0	2.0
La Perouse	-10.7	76.3	77	H	LI	0.5	1.0
Langrenus	-8.9	61.1	127	HM	E	≤0.5	2.0
Moretus	-70.6	-5.8	111	H	E (8)	≤0.75	≤1.5
Pearce	18.3	53.5	18	M	E (10)	—	≤2.0
Petavius	-25.1	60.4	188	H	EI	≤1.5	≤2.0
Piazz-Smyth	41.9	-3.2	13	M	E (11)	—	≤2.0
Picard	14.6	54.7	22	M	E (12)	—	≤2.0
Plinius	15.4	23.7	43	M	E	—	≤2.0
Reiner <sup>c</sup>	7.0	-54.9	29	M	E	—	≤4.0
Schluter	-5.9	-83.3	89	H	LI	≤1.0	≤2.0
Scoresby	77.7	14.1	55	H	E	≤1.0	≤2.0
Taruntius	5.6	46.5	56	H	C	<1.0	≤2.0
Theophilus <sup>c</sup>	-11.4	26.4	110	HM	E	≤1.0	1.5
Timocharis	26.7	-13.1	33	M	E	0.6	≤2.0
Zucchius	-61.4	-50.3	64	H	C (8)	≤1.0	≤1.5

<sup>a</sup>H, highlands; M, mare; HM, at or near highland-mare boundary.

<sup>b</sup>EI, Early Imbrian; LI, Late Imbrian; E, Eratosthenian; C, Copernican; ages from *Wilhelms* [1987] except where indicated: 1, *Wilhelms* [1980]; 2, *Carr* [1966]; 3, *Wilshire* [1973]; 4, *Scott et al.* [1977]; 5, *Lucchitta* [1972]; 6, *McCauley* [1967]; 7, *Saunders and Wilhelms* [1974]; 8, *Wilhelms et al.* [1979]; 9, *Moore* [1967]; 10, *Casella and Binder* [1972]; 11, *Page* [1970]; 12, *Olson and Wilhelms* [1974].

<sup>c</sup>Defined as width beyond crater rim in units of crater radius ( $r_c$ ); dash indicates bright halo either nonexistent or cannot be resolved.

<sup>d</sup>Defined as width beyond bright halo in units of crater radius ( $r_c$ ).

<sup>e</sup>Originally identified by *Thompson* [1974].

<sup>f</sup>Hainzel A is nearly concentric with Hainzel and Hainzel C; halo is associated with one or more of these.

sizes, and whether they can provide clues for inferring the relative ages of impact craters.

[3] Radar observations at a range of wavelengths have previously been used in conjunction with other remote and in situ data sets to investigate the physical properties of the lunar regolith in the vicinity of impact craters. For example, *Thompson et al.* [1981] used Earth-based radar and infrared eclipse temperature data to investigate bright 3.8-cm radar returns that surround many impact craters. Those workers concluded that radar observations of crater ejecta provide information about the rates of degradation of surface and subsurface blocks by meteoroid bombardment, and in some cases provide a more reliable indicator of relative crater age than optical methods. In addition, craters with haloes of distinctly low 70-cm radar returns have been noted in previous work; *Thompson et al.* [1970] and *Thompson* [1974] noted that ten nearside impact craters (Table 1) show

radar-dark haloes that extend 1/4 to 2 crater radii beyond the radar-bright crater rim. These two studies interpreted the low 70-cm returns to indicate the presence of an ejecta layer lacking meter-sized rocks or boulders that would efficiently scatter the incident radiation. In addition to radar observations, Earth-based or orbital thermal infrared measurements can provide independent information about the particle size distribution at the upper surface of the lunar regolith. For example, *Schultz and Mendell* [1978] compared nighttime thermal measurements from the Apollo 17 Infrared Scanning Radiometer (ISR) with the 70-cm radar data presented by *Thompson* [1974] for a number of craters; for Aristarchus, they found that though regions of anomalously high temperatures are spatially correlated with regions of high 70-cm radar return, the radar-dark halo region noted by *Thompson* [1974] lacks the anomalous thermal signature, implying a lower density of blocks >30 cm in diameter on

the surface in that area. Though the Aristarchus region is the only region for which *Schultz and Mendell* [1978] directly compare ISR thermal data with radar-dark haloes, the relationship between thermal and radar data, and their implications for rock abundances and size distributions surrounding many other craters, are addressed in that work. These results illustrate the utility of complementary use of optical and thermal data sets and Earth-based radar measurements for examining the physical properties of the regolith.

[4] Radar observations have also been used to investigate other aspects of the lunar regolith, including the extent and nature of pyroclastic deposits [e.g., *Zisk et al.*, 1977; *Gaddis et al.*, 1985] and chemical variations within the maria [e.g., *Schaber et al.*, 1975]. The latter study compared depolarized radar returns at 3.8-cm and 70-cm with geologic, photometric, and VIS/IR data to investigate correlations of low radar backscatter with stratigraphically distinct lava flow units in Mare Imbrium. These workers observed that lower radar returns are correlated with increased ilmenite abundance, and concluded that radar absorption increases with ilmenite content. Later, *Campbell et al.* [1997] investigated six nearside maria using radar measurements at 70 cm and 7.5 m, and found that variations in regional 70-cm depolarized echoes are inversely related to variations in regolith TiO<sub>2</sub> abundance. These two studies suggest that Earth-based radar observations can be used to augment spectroscopic data to differentiate certain chemically distinct units, in addition to their utility for characterizing variations in regolith physical properties (such as block size distribution).

[5] It should be noted that the radar-dark haloes examined in the present study are different from the “dark-haloed craters” that result from impacts into buried mare material or from volcanism [e.g., *Hawke and Bell*, 1981; *Wilhelms*, 1987], and which appear dark in optical data sets. The features examined in our study specifically show low radar reflectivity at 70-cm wavelength. This characteristically low radar return could result from (1) the presence of a regolith component with higher loss tangent than the surrounding terrain or (2) the presence of a relatively block-poor mantling deposit produced by the impact process [*Oberbeck*, 1975; *Schultz and Mendell*, 1978; *Schultz and Gault*, 1985]. In this paper, we use 70-cm radar observations in conjunction with multispectral data to distinguish between these two possible mechanisms. In the following sections, we first introduce the radar data and the craters investigated in this study. Next, we discuss the interaction of radar with the lunar regolith and examine in more detail the two candidate mechanisms for formation of radar-dark crater haloes. Finally, we present results for highland and mare craters and discuss their implications.

## 2. Radar-Dark Halo Craters

[6] We conducted a survey of craters with radar-dark haloes using the 70-cm radar observations made during 1981–1984 at the Arecibo radio telescope [*Thompson*, 1987] and more recent data obtained in 2000, 2003, and 2004. The 1981–1984 mosaic represents the most spatially complete database of P-band radar observations and is calibrated to an average lunar backscatter value determined by slowly sweeping the antenna beam across the Moon

[*Thompson*, 1987]. The spatial resolution of those data is 2–5 km, and varies across and among the individual scenes that compose the mosaic. The 2003 and 2004 observations were collected in a bistatic configuration, using the Arecibo telescope to transmit a 3- $\mu$ s uncoded signal and the Greenbank, West Virginia 105-m radiotelescope to receive both opposite-sense and same-sense polarized (specifically, LR and LL) signals. The observations obtained in 2000 were collected in a monostatic configuration using the Arecibo radiotelescope to collect opposite-sense (LR) signals. These newly acquired scenes are composed of 4–6 looks, focused to minimize smearing due to motion of points relative to the pointing target, and resampled at  $\sim$ 400 meters/pixel spacing. The locations of the craters investigated here are plotted on the hemispheric 1981–1984 radar mosaic in Figure 1.

[7] *Thompson* [1974] identified ten nearside craters as showing radar-dark haloes extending beyond the radar-bright crater rim material from 1/4 to 2 crater radii: Aristoteles, Aristillus, Aristarchus, Bullialdus, Galilaei, Galilaei A, Plato, Plato J, Reiner, and Theophilus. We began our survey of nearside craters with these ten using the higher-resolution 1981–1984 data, then expanded our survey to include the entire nearside (Table 1). The features of interest are low-return haloes that are clearly associated with their respective craters; in most cases, the haloes are fairly uniform in radar return and are distinctly darker (2–6 dB, or darker by a factor of 1.6–4) than the surrounding terrain, both in the 1981–1984 mosaic and the recently acquired observations. On the basis of the high-resolution data now available, we conclude that three of the ten original craters (Aristillus, Plato, and Plato J), may have only fortuitous haloes; that is, boundaries in echo strength in the regions surrounding the craters clearly exist but are not directly associated with crater materials. This is true of a number of other nearside craters as well. The dark regions in these cases commonly extend farther than the typical radar-dark halo dimensions listed in Table 1, or form large contiguous dark regions that extend across the surrounding terrain in one or more directions. In some cases, these dark regions correspond to patches of smooth mare material; in others, they are mare flow boundaries visible in the radar imagery that because of their serendipitous planform, appear in low-resolution images as crater haloes. The craters listed in Table 1 represent those for which we have identified radar-dark haloes that appear to be clearly related to crater materials. Our survey resulted in identification of 39 such craters spanning a wide range of sizes, with diameters of 9 to 188 km. These craters occur across the full range of lunar physiographic settings, including maria, highlands, and at highland-mare boundaries.

[8] In order to explore the origins of the radar-dark haloes, we must understand how radar interacts with the lunar regolith. In the next section, we discuss the factors that control the strength and polarization characteristics of the radar returns, and ways in which the two candidate mechanisms for formation of radar-dark haloes can be distinguished.

## 3. Radar Interaction With the Lunar Regolith

[9] In the most general case, the radar backscatter coefficient,  $\sigma^0$ , of the lunar regolith is composed of echoes from

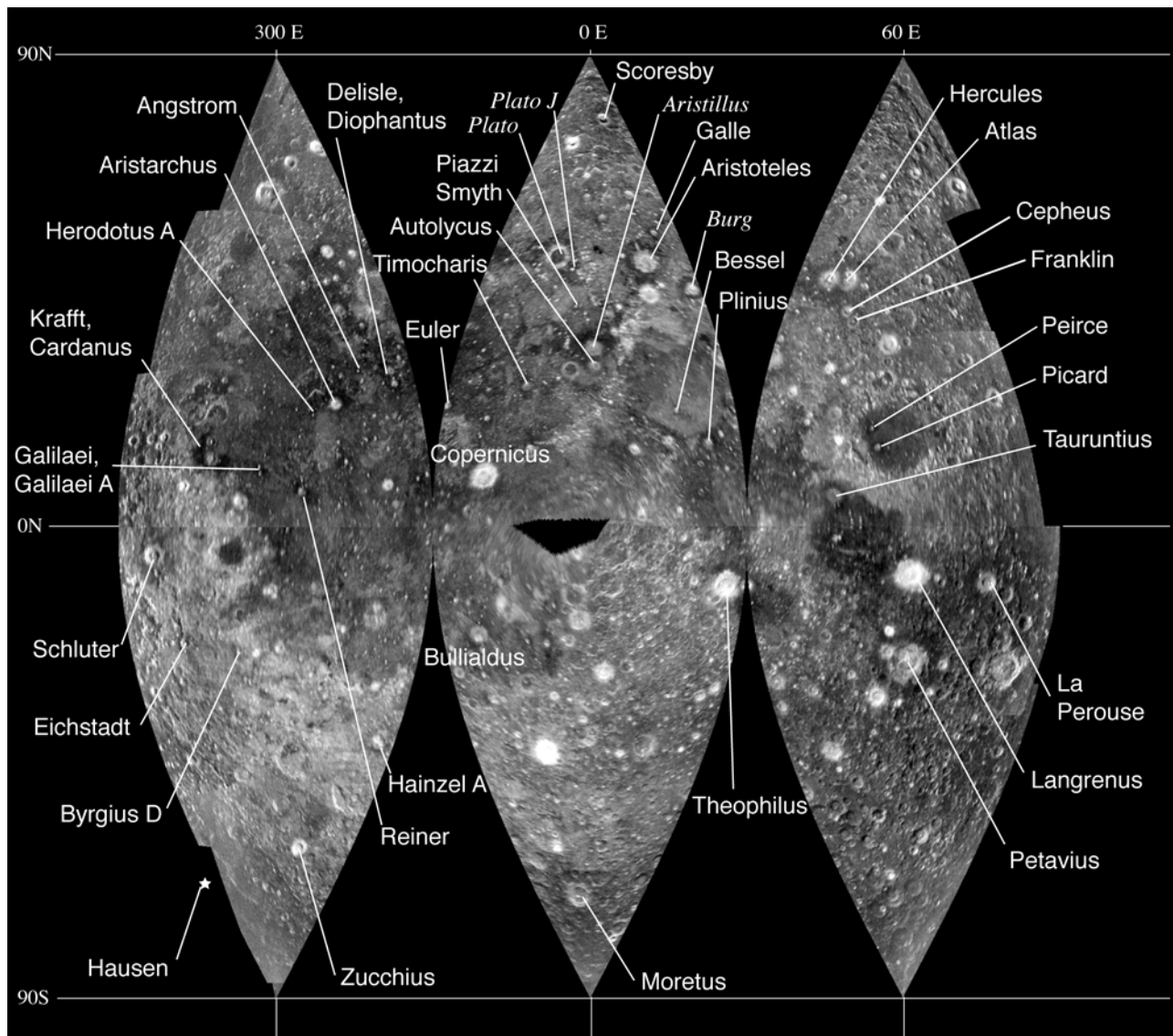


**Figure 1.** Hemispheric 1981–1984 70-cm same-sense polarized (LL) radar mosaic [see *Thompson, 1987*] (data from volume NASA-PDS\_MG\_1001) showing locations of craters with radar-dark haloes addressed in this study. Spatial resolution 2–5 km; each sinusoidally projected segment covers 60 degrees of longitude and 90 degrees of latitude. Craters labeled in italics are those whose haloes are not clearly associated with crater materials.

the surface, rocks suspended within the fine-grained matrix, and a possible basal regolith interface. The relative importance of each of these components varies with radar wavelength and is a function of surface roughness, surface and volume rock populations, the depth and dielectric properties of the matrix, and the roughness of the basal substrate. Scattering from surface topography and rocks dominates the echo at short wavelengths, whereas longer wavelength echoes (e.g., the 70-cm wavelength used here) are also sensitive to larger surface blocks and those buried within the regolith. Scattering from surface rocks is most efficient for rocks ranging roughly from 1/10 to 10 wavelengths; thus 3.8-cm radar is sensitive to centimeter-sized surface rocks, whereas 70-cm radar is sensitive to meter-sized surface blocks. Incident radar energy penetrates the

target material to a depth determined by the wavelength of the radar and the loss tangent of the material. Thus the echo at a particular wavelength represents the depth-integrated regolith properties over the radar path length. Scattering from a subregolith interface is likely weak except in cases of thin, low-loss regolith. Such a situation is likely only for young, low-titanium mare units; in older, more lossy maria or in the highlands the expected depth of the regolith is comparable to or greater than the penetration depth of a 430-MHz (70-cm wavelength) signal, which ranges up to a maximum of  $\sim 7$  meters [*Campbell et al., 1997; Campbell, 2002*].

[10] Reflections of a circularly-polarized wave from a perfectly reflecting, or specular surface, are reversed in polarization relative to the transmitted wave (e.g., left-

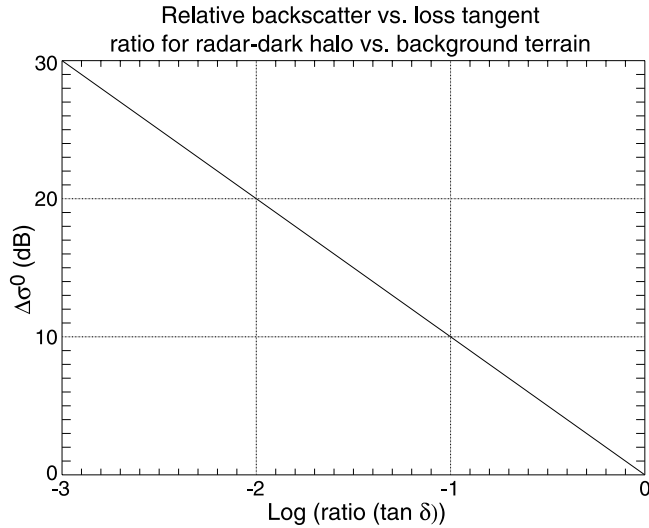


**Figure 2.** Plot of relative backscatter versus loss tangent ratio for two terrains with identical rock population densities and different loss tangents calculated according to equations (2) and (3).

circular transmit, right-circular receive). A circularly polarized wave incident on a medium with surface or subsurface scatterers comparable in dimension to the incident wavelength experiences a degree of polarization randomization, so that some of the returned energy has the same polarization as the incident wave (e.g., left-circular transmit, left-circular receive). Thus a circularly polarized wave reflected from the lunar surface consists of an opposite-sense (“OC”) and a same-sense (“SC”) component. The OC return at 70 cm is stronger than the SC component, and at low incidence angles is dominated by quasi-specular surface reflections, whereas the SC component is dominated by diffuse scattering from surface and subsurface rocks. If the regolith thickness exceeds the radar penetration depth (so that we may ignore scattering from a basal interface), we may use variations in these two components to constrain the changes in mineralogy or rock population required to produce a particular change in backscatter.

### 3.1. Changes in Mineralogy

[11] For the hypothetical case in which changes in mineralogy are responsible for the observed contrasts in echo strength, we assume that the volumetric size-frequency distribution of comminuted rocks,  $N(d)$ , is uniform between the dark halo regions and the surrounding terrain. We may express the backscatter ratio between halo and background terrain as

$$\frac{\sigma_{HALO}^o}{\sigma_{BACKGROUND}^o} = \frac{[\sigma_{SURFACE}^o + \sigma_{HALO-SUBSURFACE}^o]}{[\sigma_{SURFACE}^o + \sigma_{BACKGROUND-SUBSURFACE}^o]}, \quad (1)$$

where the surface echo is independent of the loss properties of the fine component of the regolith. The change in subsurface return is dominated by the value of the imaginary component of the dielectric constant ( $\epsilon''$ ); changes in the real dielectric constant ( $\epsilon'$ ) are linked

primarily to density, which varies only modestly with the mineralogical changes considered here. For an optically thick layer, the dependence of subsurface backscatter on dielectric constant and rock population is [Campbell, 2002]

$$\sigma_{SUBSURFACE}^o = \frac{T \cos \theta}{4\alpha} \int_{d_{min}}^{d_{max}} \sigma(d')N(d')dd', \quad (2)$$

where  $T$  is the transmission loss for the round-trip passage through the upper interface,  $\theta$  is the transmitted angle within the regolith, and  $\sigma(d)$  is the backscatter cross section ( $m^2$ ) for a rock of diameter,  $d$ . The loss factor  $\alpha$  is given by [Ulaby *et al.*, 1982]

$$\alpha = \frac{\pi\sqrt{\epsilon}}{\lambda} \tan \delta, \quad (3)$$

where  $\lambda$  is the free-space wavelength,  $\epsilon$  is real dielectric constant, and  $\tan \delta$  is the ratio of the imaginary part to the real part of the dielectric constant,  $\epsilon''/\epsilon'$ . If the rock population is invariant between the radar-dark halo and the background terrain, then the change in echo with loss tangent, in dB, is proportional to the change in the ratio of halo to background  $\tan \delta$  (Figure 2).

[12] The variability of loss tangent with mineralogy may be estimated from lab studies of the Apollo lunar samples [Carrier *et al.*, 1991]. According to that study, the scatter in loss tangent measurements is least for Apollo 15–17 samples, for which the variation in  $\tan \delta$  with bulk oxide content is approximately

$$\log_{10}(\tan \delta) = 0.03(\%TiO_2 + \%FeO) - 2.699. \quad (4)$$

Analysis of 70-cm radar data suggests that variations in ilmenite content are the primary cause of backscatter changes across the maria [Campbell *et al.*, 1997]. Since the formula for ilmenite is  $FeTiO_3$ , we may write the change in backscatter as

$$\left( \frac{\sigma_{HALO-SUBSURFACE}^o}{\sigma_{BACKGROUND-SUBSURFACE}^o} \right) = 10^{0.06(\%Ilmenite_{HALO} - \%Ilmenite_{BACKGROUND})}. \quad (5)$$

Thus each 1% increase in ilmenite content leads to a 0.6 dB reduction in the subsurface backscatter coefficient of the halo.

[13] This result represents the maximum possible change in the observed backscatter for the case of an entirely subsurface return. As the surface echo (1) increases, the impact of variation in regolith loss tangent on the observed return is reduced. If, for example,  $\sim 50\%$  of the radar echo at 70-cm wavelength comes from the subsurface (e.g.,  $\sigma_{SUBSURFACE}^o = \sigma_{SURFACE}^o$  for the reference background terrain), equation (1) becomes

$$\frac{\sigma_{HALO}^o}{\sigma_{BACKGROUND}^o} \approx \frac{1 + 10^{0.06(\%Ilmenite_{HALO} - \%Ilmenite_{BACKGROUND})}}{2}. \quad (6)$$

For this situation, a 1% change in the ilmenite content of the regolith will produce only a 0.3 dB decline in observed

return. For the observed echo variations of 2–6 dB, the required change in ilmenite abundance is quite large and should be reflected in Clementine multispectral data.

### 3.2. Changes in Rock Population

[14] Scattering from surface or subsurface rocks contributes a diffuse component to both the same-sense and the opposite-sense returns. Thus variations in rock population may result in changes in the backscatter strength. A comminuted rock population has a volumetric size-frequency distribution that is typically well described by a power law function with an exponent near  $-4$ :

$$N(d) = C_V \left( \frac{d}{d_0} \right)^{-4}, \quad (7)$$

where  $d_0$  is a reference scale, typically taken to be 1 m, and  $C_V$  is a scaling coefficient with units of  $\text{m}^{-3}$ . This corresponds to a surface rock population (units of  $\text{m}^{-2}$ ) with a power law exponent of  $-3$  [Turcotte, 1992]. If the power law exponent is held constant, then backscatter variations are linearly related to changes in  $C_V$  (e.g., a twofold decrease in  $C_V$  produces a 3 dB reduction in  $\sigma^o$ : (2)). This mechanism can be very effective, since it affects both the surface and subsurface returns. It is reasonable to expect that significant variations in  $C_V$  may occur, even in “smooth” mare terrains; for instance, best-fit volumetric rock population curves for the Surveyor 5 and 6 landing sites, for which the power law exponents are similar, have  $C_V$  values that differ by a factor of  $\sim 3.5$  [Campbell, 2002]. Both these landing sites are characterized by smooth terrain with relatively few large blocks, and are quite similar in appearance and general character, yet a difference in  $C_V$  of 3.5 would result in a reduction in  $\sigma^o$  of nearly 5.5 dB, if the exponents were identical. Larger variations in  $C_V$  likely occur in association with ejecta material from large impact craters. The observed echo variations of several dB can thus be explained with reasonable variations in rock population.

### 3.3. Polarization Ratio

[15] In addition to diffuse scattering from rocks, the opposite-sense return is also sensitive to quasi-specular reflections from surface or basal topography or rock faces on scales larger than the radar wavelength. The circular polarization ratio,  $\mu_c = \sigma_{sc}^0 / \sigma_{oc}^0$ , provides an estimate of the relative importance of diffuse versus quasi-specular return. Very blocky terrain may show high (approaching unity) values of  $\mu_c$ . As rock abundance declines, the diffuse component decreases rapidly relative to the quasi-specular component; thus the same-sense echo decreases more rapidly than the opposite-sense echo, resulting in low values of  $\mu_c$  and exaggerating the contrast between the radar-dark haloes and the surrounding terrain. This enables a more detailed examination of the geometries and spatial relationships of the dark haloes with other crater materials and the surrounding terrain than is possible using either the polarized or depolarized data alone. The color-coded map of circular polarization ratio overlain on the 1981–1984 OC mosaic in Figure 3 shows high values of  $\mu_c$  near young blocky craters such as Tycho, whereas the radar-dark haloes

appear as rings of low  $\mu_c$  surrounding their respective craters.

## 4. Results and Interpretations

[16] Our survey resulted in identification of 39 nearside craters with radar-dark haloes (Table 1); 14 of these reside in the highlands, 16 in the maria, and 9 are located at or near highlands-mare boundaries. We discuss the highland and mare craters separately; the highland-mare boundary craters are included in one of these two categories depending on whether they are located in dominantly mare or highland terrain. For example, both Aristarchus and Copernicus (listed in Table 1 as highland-mare boundary craters) are located in mare regions where the mare fill is relatively thin and some highland terrain is exposed, so are grouped in this analysis with the mare craters. On the other hand, the terrain surrounding Langrenus dominantly consists of cratered highlands with smaller mare areas represented, so Langrenus is grouped with the highland craters.

### 4.1. Highland Craters: Radar Characteristics

[17] The highland craters listed in Table 1 range from 28–188 km in diameter. Several of these craters are shown in Figure 4, which shows new (collected in 2003 and 2004) dual-polarization observations of the southern hemisphere. Each of these craters shows a low-return halo in the SC images that contrasts clearly with the background highland terrain and has distinctly low values of  $\mu_c$  relative to its surroundings. The southern highlands are characterized by many additional small craters with less distinct dark haloes; identification of haloes is challenging in this part of the Moon because the highland terrain varies widely in radar brightness. Clear identification of a radar-dark halo requires a crater of sufficient size for the associated deposits to superpose an appreciable number of other craters or topographic features. This is the case for Schluter (Figure 4a) and for Petavius (Figure 4c), which show distinct dark haloes in both the SC and the polarization ratio images. The halo associated with Schluter extends across the outermost ring of the Orientale basin (Montes Cordillera) and onto the surrounding terrain. Petavius’ halo, which has a smooth margin and symmetric shape, superposes many older craters and is superposed by several younger craters. Some of these younger craters (e.g., Stevinus, Wrottesley, Petavius B) may have haloes of their own, but identification of such is difficult because these craters lie almost completely within Petavius’ distinctive halo.

[18] Comparison of the 70-cm radar images with Apollo and Lunar Orbiter images and with lunar geologic maps shows that for most of the large craters ( $d > 50$  km) with radar-dark haloes, the proximal, radar-bright portions of the ejecta are associated with an annulus of hummocky ejecta deposited immediately outside the crater rim; this observation is consistent with the findings of Schultz and Mendell [1978], which are based on Apollo ISR data. These deposits show radar returns similar to or brighter than the surrounding terrain at a range of radar wavelengths [Thompson et al., 1981], indicating roughness at centimeter- to meter-scales (Figure 5). By contrast, the 70-cm radar-dark haloes are to some degree spatially correlated with more distal ejecta deposits characterized by elongate ridges trending radial or

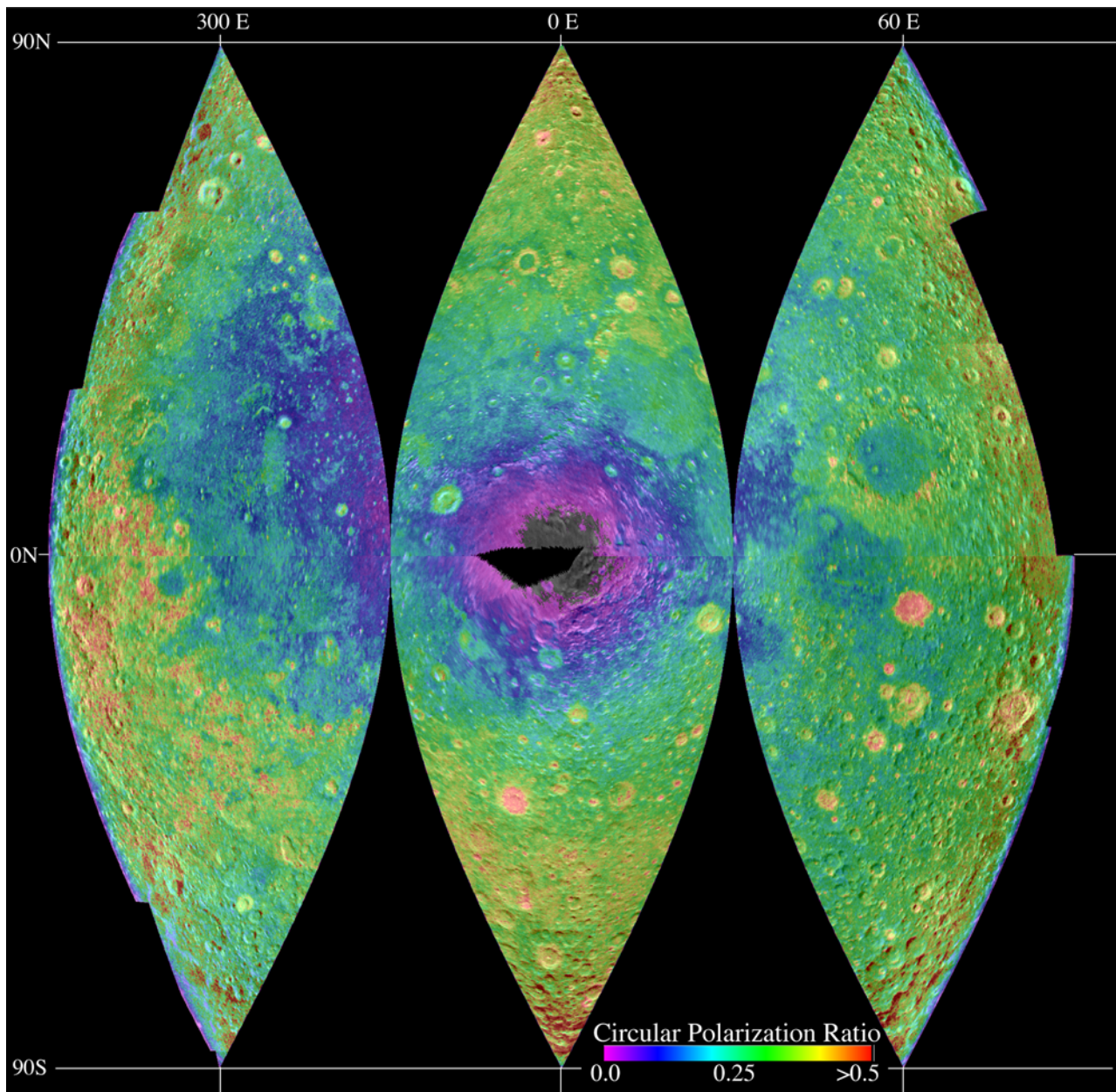


**Figure 3.** Color-coded circular polarization ratio map overlain on hemispheric 1981–1984 70-cm OC radar mosaic [see *Thompson, 1987*] (data from volume NASA\_PDS\_MG\_1001); sinuoidally projected segments are  $60 \times 90$  degrees. The circular polarization ratio was calculated from observed power with no correction for the beam pattern; this causes the low values of  $\mu_c$  near the center of the moon. Dark-haloed craters examined in this study (compare with Figure 1) show low values of  $\mu_c$  relative to the surrounding terrain.

subradial to the craters, by hummocky topography, and by secondary impact features. The correspondence of these types of deposits with the dark haloes is most clearly apparent where the ejecta deposits and the radar-dark haloes both show asymmetry, a relationship that is more common for mare craters than for those in the highlands. For smaller craters and for those that are located in areas of rugged topography related to large basins such as Orientale, the relationships between mapped ejecta deposits and the radar-dark haloes are not well defined.

[19] Radar images at 3.8-cm wavelength [*Zisk et al., 1974*] do not show distinct radar-dark haloes corresponding to those visible at 70-cm. For example, 3.8-cm radar mosaics for Petavius (Figure 5) show average to bright radar returns corresponding with material surrounding nearby young craters, but no patterns that correspond with the radar-dark halo observed at 70-cm. This indicates that the mechanism(s) responsible for the presence of low-return haloes in 70-cm wavelength images does not produce a similar effect at 3.8-cm. We expand on this point at the end of the next section.

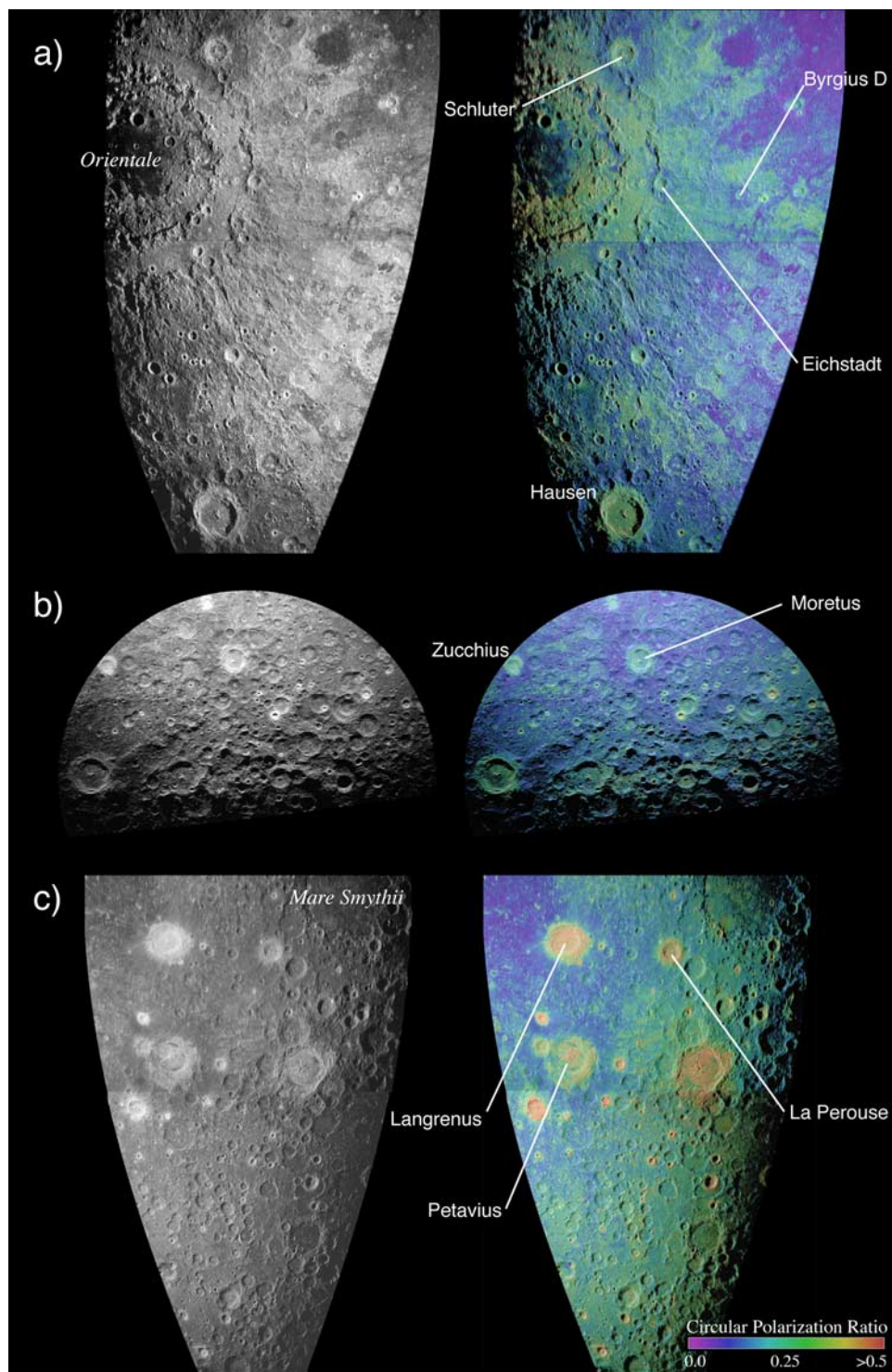


**Figure 4.** Dual polarization 70-cm radar images acquired in 2000, 2003, and 2004; same-sense (LL) polarized (left) and color-coded circular polarization ratio overlain on opposite-sense (LR) data (right); north is at top. Offsets in mosaics result from contrasts across scene boundaries; no beam pattern or scattering law corrections have been applied. Labeled craters show low-return haloes in SC images and low  $\mu_c$  values in ratio images. (a) Mosaic of Orientale region (0–70S, 260–310E); (b) south pole mosaic (~60–90S, 260–100E; radar sees slightly past the pole); (c) mosaic of Petavius region (0–70S, 50–100E).

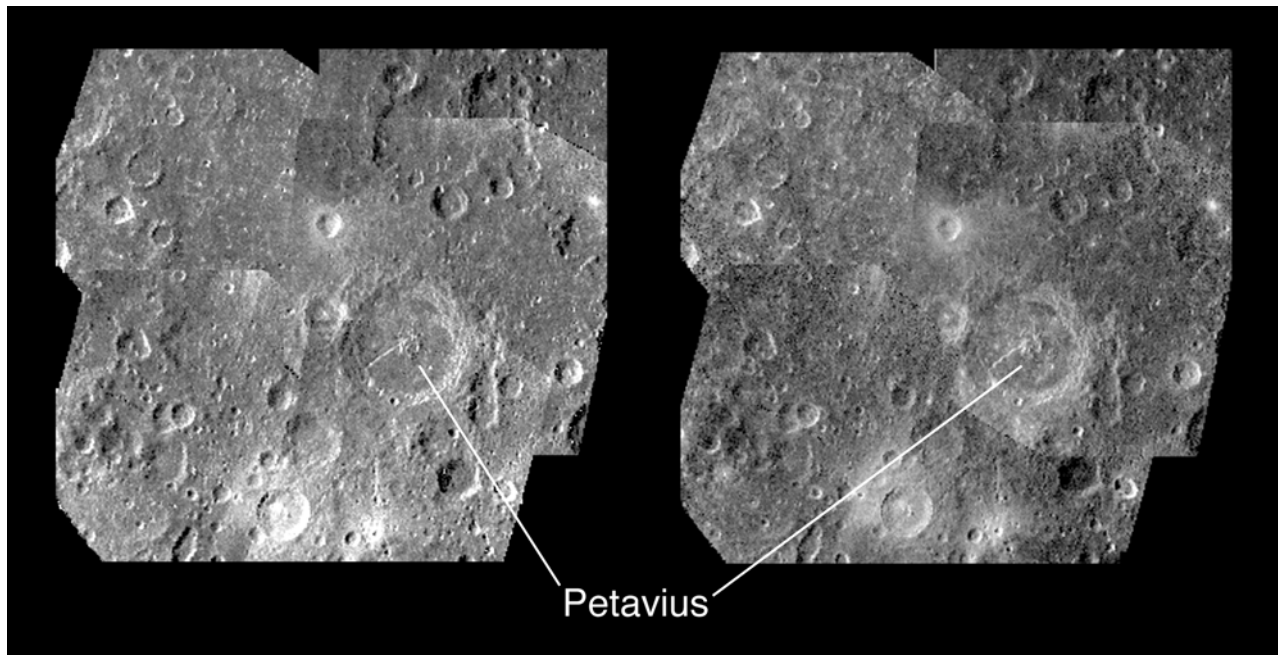


**Figure 5.** Radar mosaics of Petavius at 3.8 cm wavelength [see Zisk *et al.*, 1974] (data from volume NASA\_PDS\_MG\_1001): (left) OC and (right) SC. Note absence of radar-dark halo corresponding to that visible at 70-cm. North at top; diameter of Petavius: 188 km.

#### 4.2. Highland Craters: Comparison of Radar With Multispectral Data

[20] If the presence of radar-dark haloes in the highlands is controlled by the presence of lossy material (such as ilmenite) excavated from beneath the regolith, we would predict the haloes to show an enhanced  $\text{TiO}_2$  or FeO abundance. As outlined in section 3, a halo echo 3 dB lower than the background terrain should correspond to a  $\text{TiO}_2$  enhancement of 5–10 weight percent relative to the background terrain. A shift of this magnitude should be readily apparent in Clementine UV/VIS multispectral data. To examine this potential relationship, we constructed image mosaics from the Clementine data representing  $\text{TiO}_2$  content using the method of Gillis *et al.* [2003]; we also constructed FeO content and optical maturity maps using the methods of Lucey *et al.* [2000a, 2000b] for each of the craters in Table 1; the maps for the Orientale and Petavius regions (Figures 6 and 7) are shown as examples. The Orientale scene is characterized by low  $\text{TiO}_2$  abundance except for mare materials in the interior of Mare Orientale and along the interior margins of the basin rings. The two dark-haloed craters in this scene, Schluter and Eichstadt, show no enhancements in either FeO or  $\text{TiO}_2$  in the halo regions, indicating that the surface material excavated by these two craters is not high- $\text{TiO}_2$  material from below the regolith. Evidence for variations in optical maturity of the surface materials corresponding to the radar-dark haloes is similarly absent (Figure 6d; compare with Figure 4a). Additionally, the region shows an extremely homogeneous mature soil signature in three-color band ratio maps [e.g., McEwen *et al.*, 1994] and both craters appear nearly indistinguishable from the surrounding terrains, except for small exposures of fresher highland material in the crater

walls (bright in Figure 6d). The situation is similar for dark-haloed craters Petavius and Langrenus (Figure 7). The SW margin of Mare Fecunditatis is visible in the upper left corner of Figure 7, and shows a characteristically higher  $\text{TiO}_2$  abundance than the neighboring highland terrain. By contrast, the materials excavated by Langrenus, Petavius, and Petavius B have very low  $\text{TiO}_2$  content, as expected for highland material. The optical maturity image (Figure 7d) shows exposure of immature material in the walls of Langrenus and Petavius B, as well as rays of fresh material extending radially from Petavius B and overprinting Stevinus, Wrottesley, and Petavius. None of these variations in composition or maturity corresponds spatially to the geometry or extent of either Petavius' or Langrenus' radar-dark halo (Figure 4c). Variations in the chemistry or optical maturity of the surface materials do not seem to be responsible for the dark haloes in this region. This pattern persists for all of the highland craters listed in Table 1.

[21] We conclude that because enhanced  $\text{TiO}_2$  (or FeO) content is not responsible for the lower radar cross-section, low-return haloes in the highlands most likely result from variations in block population in the upper several meters of the highland regolith. As outlined in section 3.2, relatively minor variations in the power law volumetric distribution of blocks suspended in the fine regolith fraction can account for the observed offsets of several dB in radar echo power. We propose that the radar-dark haloes are evidence of a layer of ejecta dominated by fine particles that falls distal to (and after) the larger blocks that characterize the proximal crater ejecta [e.g., Schultz and Mendell, 1978; Schultz and Gault, 1985; Wilhelms, 1987; Melosh, 1996]. The depth of such a layer required to attenuate the depolarized radar

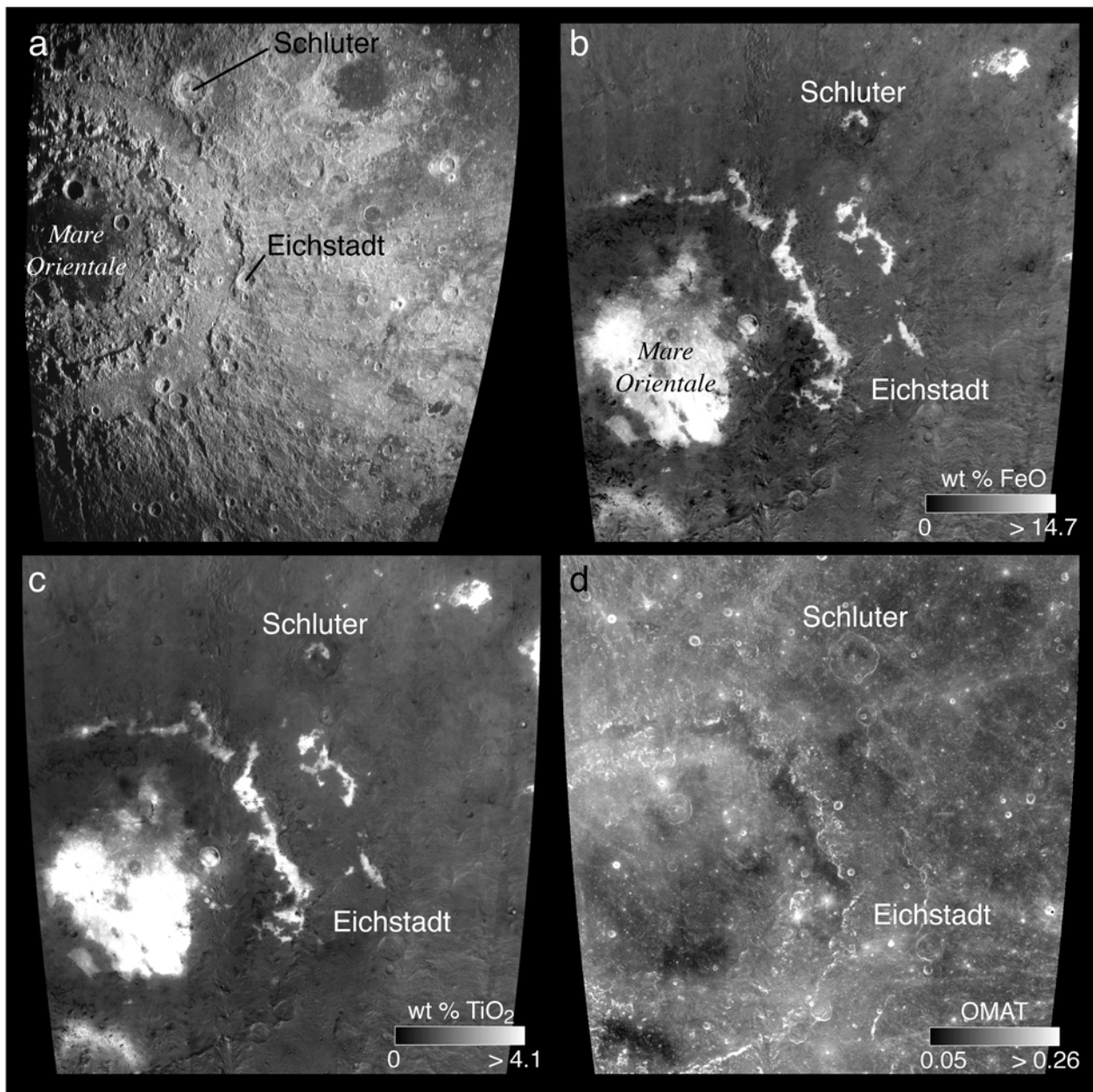


**Figure 6.** (a) 70-cm radar (SC) and (b–d) Clementine UV/VIS mosaics for the Orientale region showing dark-haloed craters Schluter (diameter = 89 km) and Eichstadt (diameter = 49 km). North is at top for all images. Radar mosaic, 0–70S, 55–105W; Clementine mosaics, 0–30S, 70–100 W; all sinusoidally projected. (b) Map of weight percent FeO [Lucey *et al.*, 2000a]. (c) Map of weight percent TiO<sub>2</sub> [Gillis *et al.*, 2003]. (d) Optical maturity index (OMAT) [Lucey *et al.*, 2000b]. The regions corresponding to the radar-dark haloes surrounding Schluter and Eichstadt show no evidence for ilmenite enhancement (expressed as FeO or TiO<sub>2</sub> content) relative to the surrounding terrain (compare with Figure 4a); likewise, there is no signature in the optical maturity image corresponding with the haloes.

signal to the observed degree is likely no more than a few meters, depending on the loss properties and particle size distribution in the layer, so does not represent an appreciable fraction of the total estimated ejecta volume for any given crater.

[22] Because cratering mechanisms are similar across a wide range of impactor and crater sizes, target materials, and impact energies, such a fine ejecta layer should pre-

sumably exist for all craters above a certain size threshold. Indeed, many more craters than those listed in Table 1, particularly those with small diameters, show some degree of evidence for dark haloes; we chose only craters above ~10 km in diameter for detailed analysis. However, not every nearside highland crater has a dark halo. Craters of Nectarian and pre-Nectarian age lack dark haloes; in fact, Petavius and Franklin, of Early Imbrian age [Wilhelms,

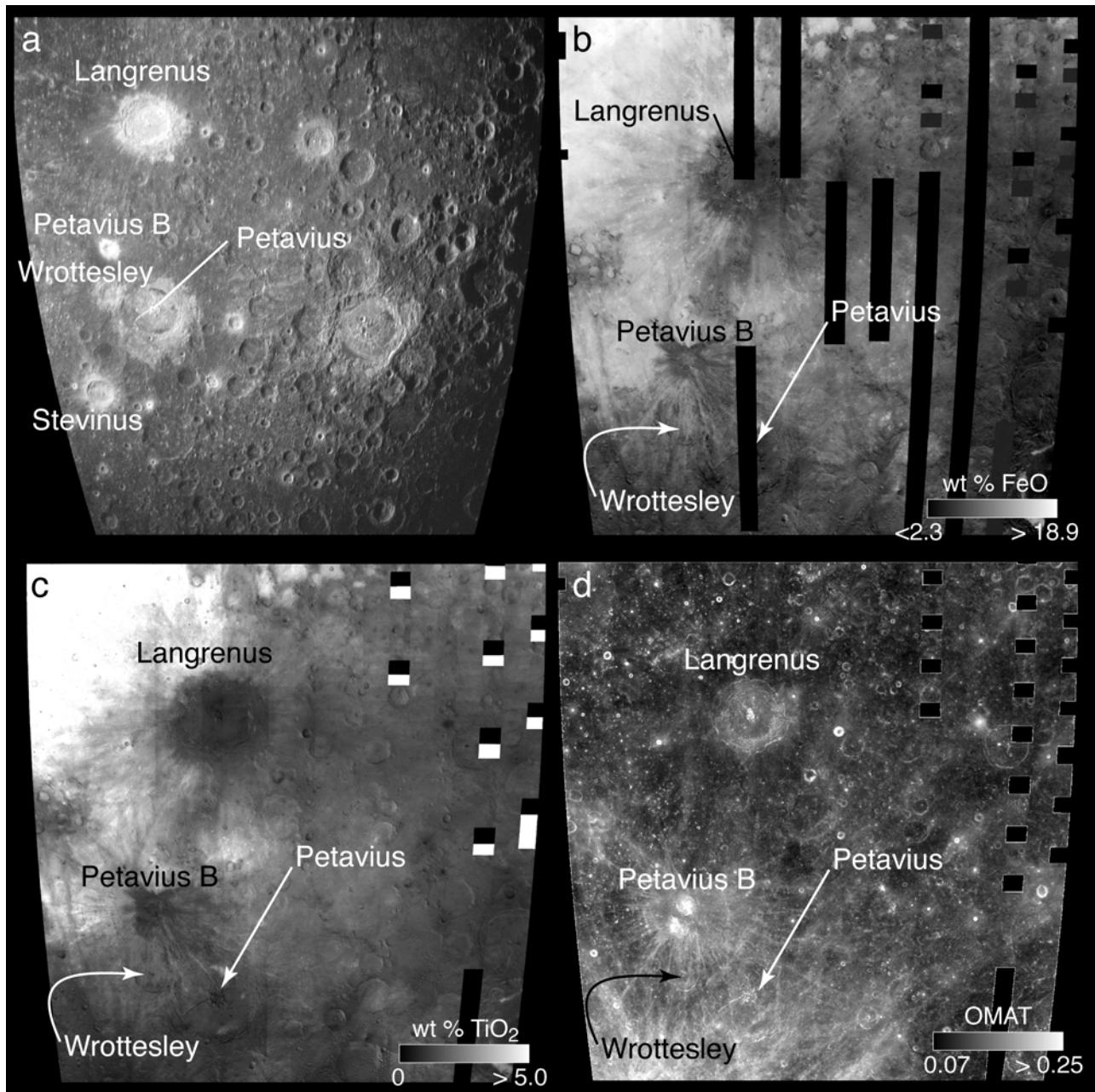


**Figure 7.** (a) 70-cm radar (SC) and (b–d) Clementine UV/VIS mosaics for the Petavius region showing dark-haloed craters Petavius (diameter = 188 km) and Langrenus (diameter = 127 km; compare with Figure 4c). North is at top for all images. Radar mosaic, 0–45S, 50–100E; Clementine mosaics, 0–30S, 50–80E; all sinusoidally projected. (b) Weight percent FeO. (c) Weight percent TiO<sub>2</sub>. (d) OMAT. As for the Orientale region, this area shows no evidence for ilmenite enhancement or variations in maturity that might account for the dark haloes evident in radar images of this region. The radial rays emanating from Petavius B indicate that fresh material has been excavated, but these materials do not seem to correspond to the dark features visible in the radar mosaic.

1987], are the oldest recognized craters with radar-dark haloes on the nearside. This suggests that the dark haloes disappear with time. Bombardment of the lunar surface by impactors of various sizes tends over time to break down large particles, and impacts of the size that produce 10–100m diameter craters act to homogenize the regolith by overturn, gardening, or brecciation. We expect that a layer of fine ejecta associated with a Nectarian or pre-Nectarian

crater would have been overprinted or obliterated by continued excavation and overturn of the surrounding regolith by the present time, such that the radar returns from the region once occupied by fine distal ejecta are now indistinguishable from those of the surrounding terrain. This process is illustrated in schematic form in Figure 8. The absence of radar-dark haloes in 3.8-cm radar images helps to constrain the depth of the fine ejecta layer, and places

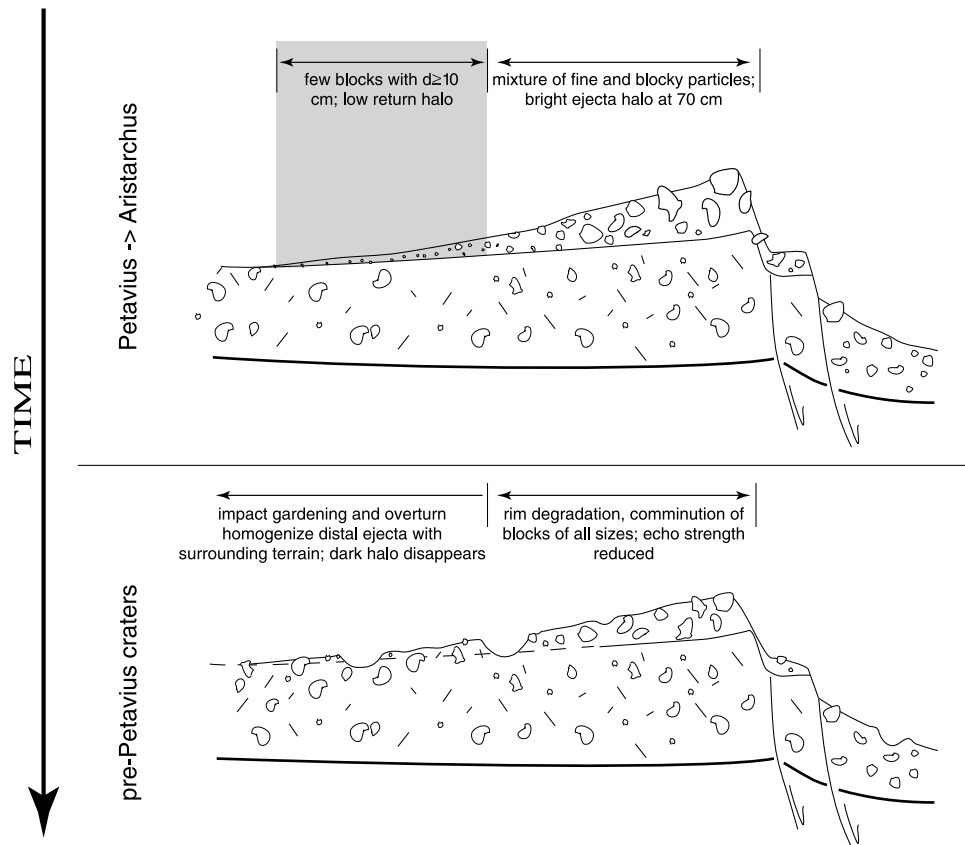


**Figure 8.** Schematic diagram showing proposed progression of distal ejecta characteristics with time. (top) Young craters (Copernican - Early Imbrian) characterized by blocky ejecta that fines with distance; distal layer depleted in decimeter- to meter-sized blocks attenuates 70-cm signals. Near the rim, ejecta is sufficiently blocky to produce bright 70-cm radar returns. (bottom) Overturn and gardening by small and larger impactors on long (Imbrian and older) timescales lead to homogenization of distal ejecta with surrounding terrain, and dark haloes disappear.

bounds on the range of particle sizes represented. Incident microwave radiation at 3.8-cm is sensitive to scatterers in the upper  $\sim 1$  meter larger than approximately  $\lambda/10$ , or roughly 0.5 cm. The 70-cm returns are sensitive to blocks and topography on approximately decimeter-scales and larger, and because longer-wavelength radiation penetrates deeper than short-wavelength radiation, represent a larger volume of regolith than the 3.8-cm returns. The fact that no radar-dark haloes exist at 3.8-cm wavelength suggests that though the fine ejecta layer responsible for the haloes is depleted in blocks larger than about 10 centimeters in diameter (at least near the surface) relative to the surrounding area, it has an abundance of 1–10 centimeter-sized blocks similar to the background terrain.

#### 4.3. Mare Craters: Radar Characteristics

[23] The mare craters listed in Table 1 range from 9 to 87 km in diameter. Radar-dark haloes are easier to identify in mare settings than in highland settings because the surrounding terrain is less heavily cratered and is more uniform in radar return. For this reason, the range of mare crater sizes included in the study extends to smaller diameters than for the highlands. Seven of the mare craters are imaged in the monostatic, OC-polarized radar observations acquired in 2000 at Arecibo. The mosaic in Figure 9 was

constructed from 5 looks resampled to 400m spatial resolution; the dark haloes associated with Aristarchus, Delisle, Diophantus, Euler, Herodotus A, Piazzzi-Smyth, and Timocharis are visible in this mosaic. Aristarchus and Herodotus A have unique characteristics discussed below. Plato and Plato J, located near the northern boundary of Imbrium and identified by *Thompson* [1974] as showing dark haloes, are also visible in this mosaic. Close examination of these new data for Plato indicates that though the crater is surrounded by dark material, it does not appear to possess the same type of dark halo as the craters of interest in this study. The radar-dark region that surrounds Plato extends well beyond the vicinity of the crater and thus may be unrelated to crater ejecta. Clear evidence for widespread volcanic activity in the Plato region suggests that some of the dark material may be volcanic ash or other volcanic products [e.g., *Schultz*, 1976; *Thompson et al.*, 1978; *Gaddis et al.*, 1985].

[24] Two additional craters, Aristillus and Bürg, that seem to show prominent dark haloes in the mosaic in Figure 1 are not included in Table 1. Detailed examination of the 1981–1984 radar data for these two craters shows that the dark area surrounding each corresponds with the boundaries of the host mare (Lacus Mortis for Bürg, and eastern Imbrium and Sinus Lunicus for Aristillus). Future acquisition of high-resolution, dual-polarization data for these craters

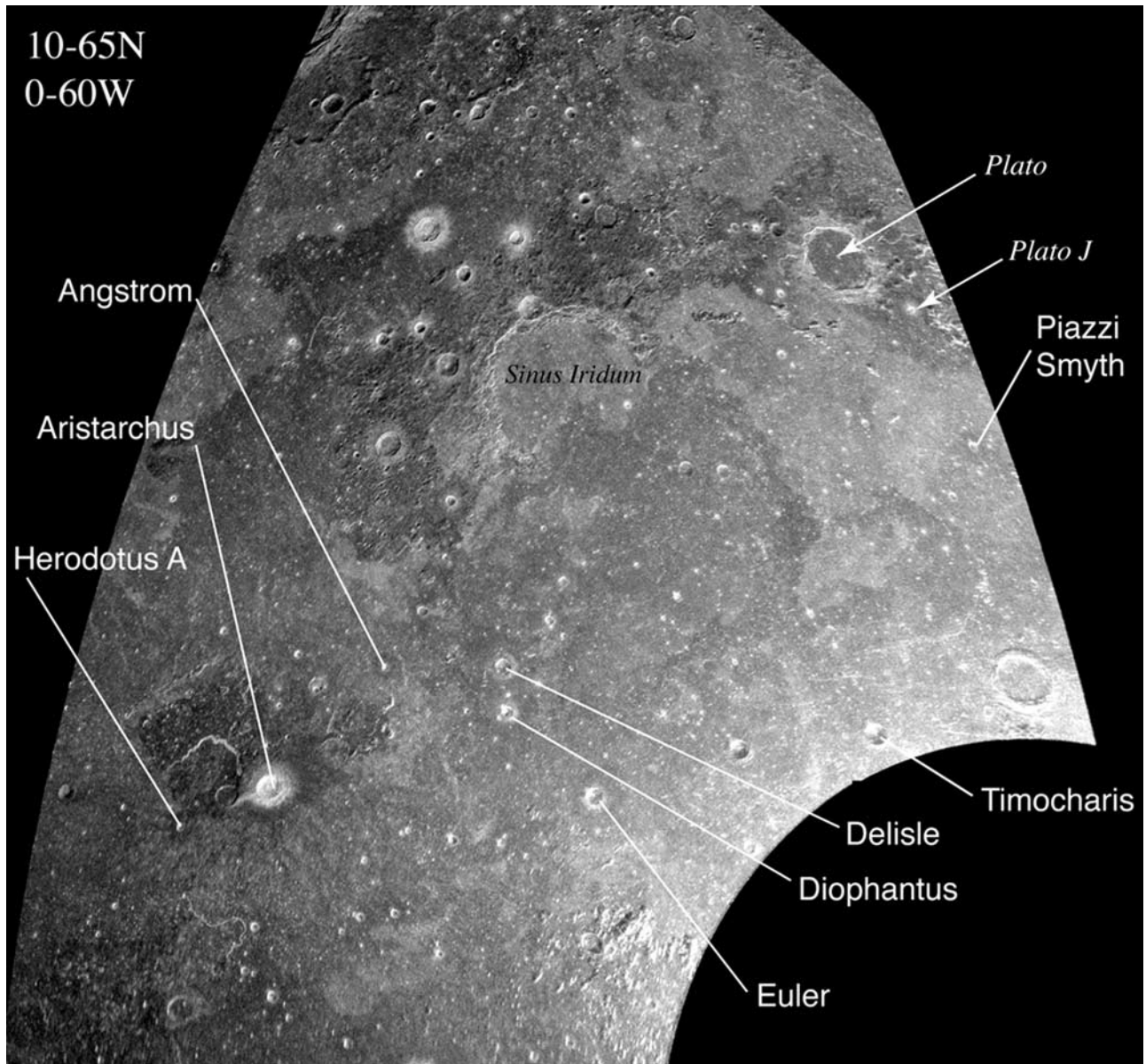


**Figure 9.** Seventy-centimeter OC radar mosaic of Imbrium region, acquired in 2000. Diameter of Aristarchus: 40 km; Plato: 109 km; Sinus Iridium: 260 km.

may show evidence for dark haloes distinct from the mare boundaries, but with the data currently available, we cannot confidently identify radar-dark haloes of the same type as for the craters listed in Table 1. As was true for the highland craters, comparison of the 70-cm radar images with Apollo and Lunar Orbiter images and with lunar geologic maps shows that the spatial patterns represented by the dark haloes commonly match those defined by radial ridged ejecta units distal to the more hummocky ejecta that characterizes the proximal, radar-bright ejecta. For some craters, both the radial ridged ejecta materials and the radar dark halo are notably asymmetric; this is commonly caused by embayment of crater ejecta by younger mare flows [e.g., *Wilhelms*, 1980]. For example, the dark halo surrounding Krafft is absent along the eastern margin of the crater but extends to 2 crater radii clockwise from south to north-

northwest. The distribution of radial ridged ejecta as visible in Lunar Orbiter frames IV-174H<sub>2</sub> and IV-169H<sub>2</sub> matches this pattern, and the missing ejecta to the east appears to have been buried by Procellarum basalt flows [*Wilhelms*, 1987]. Another asymmetric halo exists at Reiner, where a “butterfly” pattern is apparent with lobes to the NW and SE (see Lunar Orbiter frame IV-157H<sub>1</sub>). The pattern of radial ridged ejecta at Reiner matches this distribution, and may be due either to oblique impact or, more likely, embayment by younger flows [*Whitford-Stark and Head*, 1980; *Wilhelms*, 1987]. At Euler, the radial ridged ejecta are embayed by younger basalt flows [*Wilhelms*, 1980]; the spatial pattern created by this embayment relationship corresponds fairly closely to the form of the radar-dark halo (Figures 10a and 10b). In all three of these cases, likely embayment of the ejecta by younger flows creates a sharp boundary

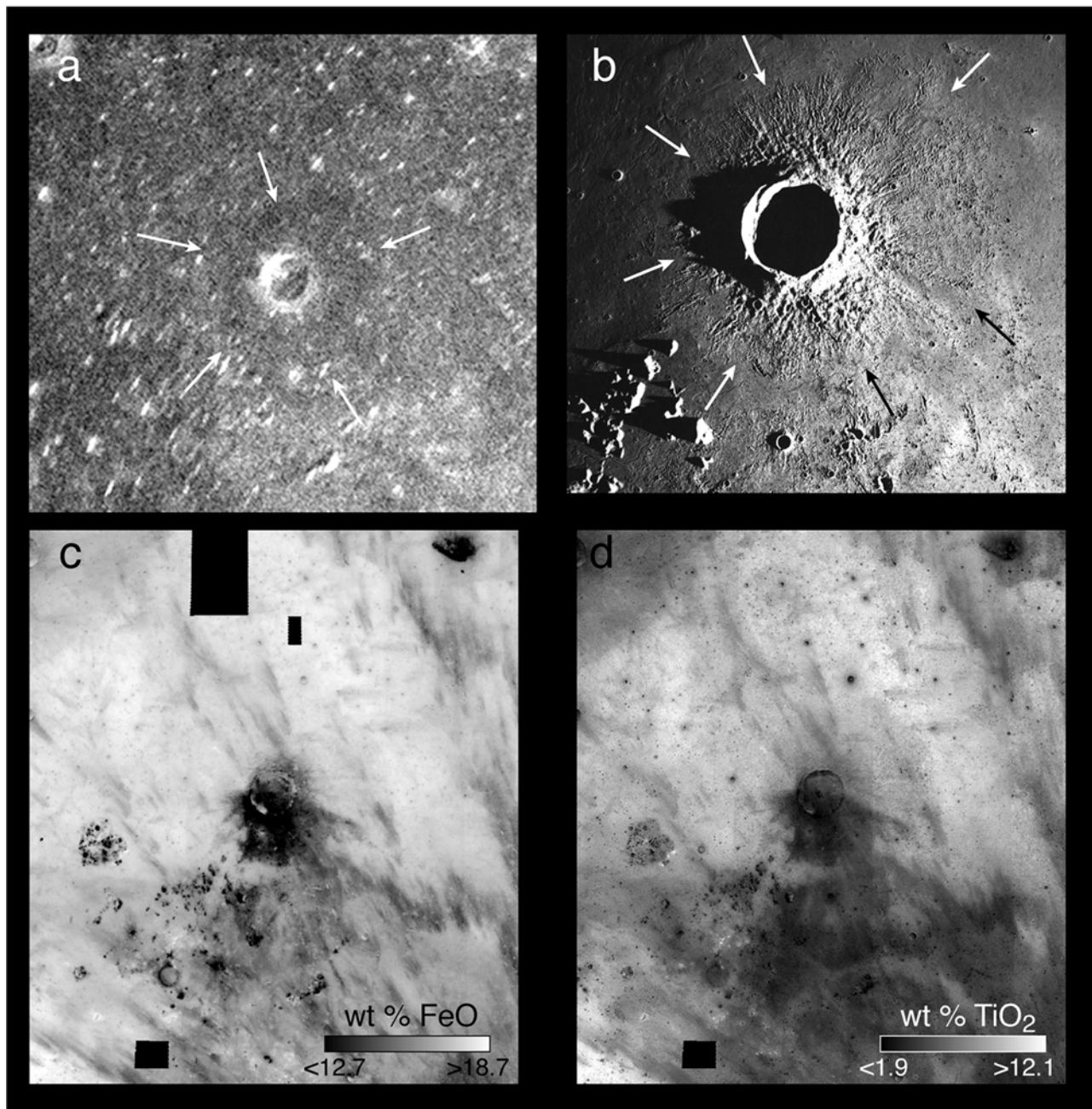


**Figure 10.** Remote-sensing images for Euler (diameter = 27 km); north is at top for all images. (a) SC 70-cm radar image, enlargement of Euler from Figure 9. Heads of white arrows denote boundaries of radar-dark halo. (b) Portion of Apollo 17 metric frame 2293; the extent of the radial ridged ejecta corresponds approximately with the boundaries of the radar-dark halo. Arrows denote boundaries of Euler ejecta and show embayment relationship with younger basalt flows [Wilhelms, 1980]. (c) Weight percent FeO. (d) Weight percent TiO<sub>2</sub>. Clementine mosaics show distinct fan-shaped pattern of material ejected from Euler. This fan-shaped feature shows anomalous values of FeO and TiO<sub>2</sub> relative to the surrounding region but does not correspond with the radar-dark halo.

associated with the radar-dark haloes, increasing their visibility in the maria. The degree to which the close relationship between the radar-dark halo and the radial ejecta deposits is apparent varies from crater to crater, and for small craters, is difficult to evaluate; however, a general correlation seems to exist between these distal ejecta materials and the distribution of radar-dark halo materials.

#### 4.4. Mare Craters: Comparison of Radar With Multispectral Data

[25] Because mare basalts are generally higher in TiO<sub>2</sub> content than highlands materials, it is reasonable to ask whether variations in composition play a role in creating radar-dark haloes associated with mare craters. To address this, we again constructed element and maturity maps from

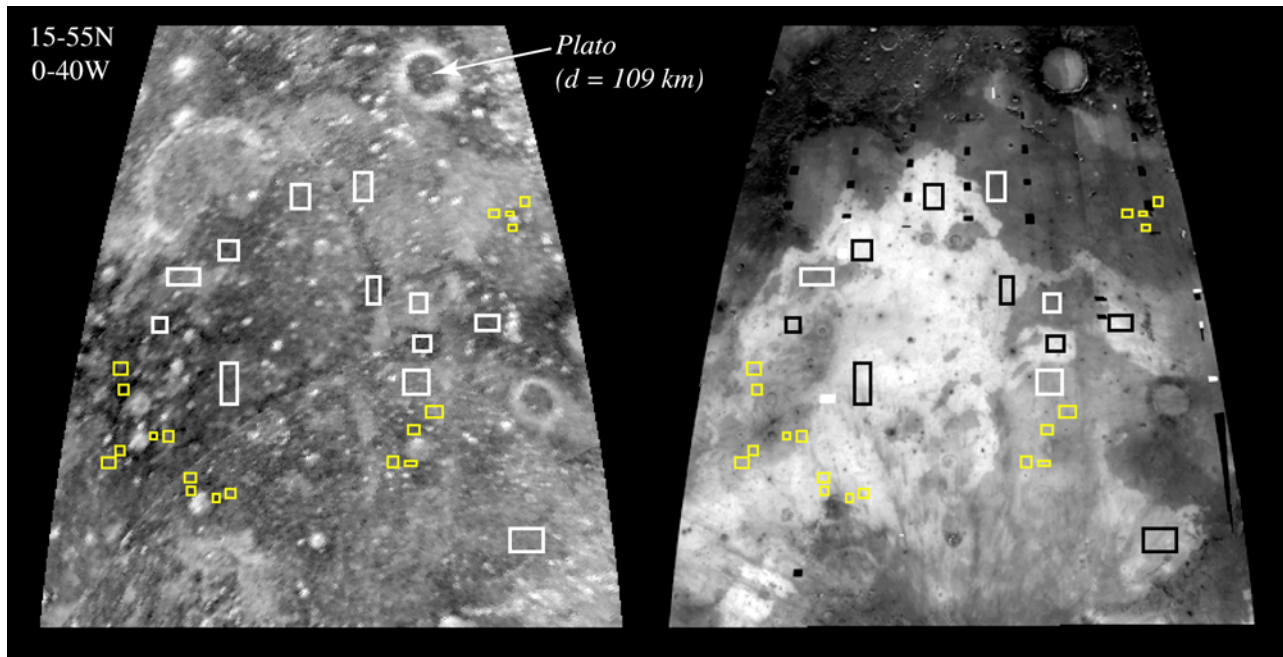


**Figure 11.** (left) Seventy-centimeter radar mosaic (SC) of Imbrium region [see *Thompson, 1987*] (data from NASA\_PDS\_MG\_1001). (right)  $\text{TiO}_2$  map of same region from Clementine UV/VIS data. North is at top. Note correlation of flow boundaries between radar and  $\text{TiO}_2$  maps. White and black boxes show areas used to calculate plots of radar power versus  $\text{TiO}_2$  content plots for Imbrium flows; yellow boxes show crater halo and background areas used for comparison with these flows (Figure 12).

the Clementine UV/VIS multispectral data for the mare craters listed in Table 1. As for the highland craters, we found for the mare craters a consistent lack of correlation between spatial variations in composition or maturity and radar-dark haloes. A particularly striking example is Euler (Figures 10c and 10d), which shows a distinct fan-shaped deposit with low  $\text{TiO}_2$  and FeO content emanating from the crater toward the south. The radar-dark halo, however, extends in all directions beyond the farthest reaches of the anomalous fan-shaped pattern in the composition and maturity maps; the radar halo does not appear to be spatially correlated with variations in composition or optical maturity for this crater. For most of the mare craters, the optical reflectance characteristics of the regolith appear more uniform than at Euler, similar to the pattern observed in the highlands.

[26] Despite the apparent lack of agreement between spatial variations in composition and radar return in the radar-dark halo regions, it is known that regional variations in 70-cm radar backscatter in the maria correlate with variations in  $\text{TiO}_2$  abundance. Previously, *Campbell et al. [1997]* compared SC-polarized radar backscatter values and  $\text{TiO}_2$  abundances for selected areas in six nearside maria and observed an inverse correlation between the two parameters for Mare Imbrium, Oceanus Procellarum, Mare Tranquillitatis, Mare Fecunditatis, Mare Crisium and Mare Serenitatis. Offsets in the absolute backscatter strength among the maria ( $\sim 3$  dB total variation) were attributed largely to variations in regolith age among the basins. These observations show that a strong relationship exists in the maria between ilmenite content and backscatter strength,

consistent with previous observations [*Schaber et al., 1975*] and laboratory studies [*Carrier et al., 1991*]. Thus, though no obvious visual correlations between  $\text{TiO}_2$  abundance and radar-dark haloes seem to exist, it is nevertheless likely that variations in  $\text{TiO}_2$  content influence the radar backscatter associated with crater ejecta to some degree. In their work, *Campbell et al. [1997]* used Clementine compositional maps [*Johnson et al., 1991; Lucey et al., 1995, 1996*] constructed prior to full calibration of the Clementine multispectral data. With fully calibrated multispectral data now available [*Lucey et al., 2000a*], we conducted comparisons for the regional mare flows similar to those made by *Campbell et al. [1997]*. We plotted the median SC radar echo versus weight percent  $\text{TiO}_2$  for each of a number of sample sites in Mare Imbrium; Figure 11 shows the SC radar mosaic and corresponding  $\text{TiO}_2$  map from which these data were taken. We selected sample sites such that the range of echo strengths and  $\text{TiO}_2$  abundances across the mare were represented, avoiding radar-bright ejecta from large craters. The plot for Imbrium (Figure 12) shows a distinct anticorrelation between mean echo strength and weight percent  $\text{TiO}_2$ , in agreement with the findings of *Schaber et al. [1975]* and *Campbell et al. [1997]*.

[27] If the radar-dark haloes are controlled at least in part by loss tangent variations due to ilmenite content, we would predict a similar inverse relationship between echo strength and  $\text{TiO}_2$  content for the halo regions. Mare materials in different basins may be offset in echo power from one another due to age variations, but the slopes of echo power versus  $\text{TiO}_2$  content plots should be similar. Likewise, plots of echo strength versus  $\text{TiO}_2$  content for materials associ-

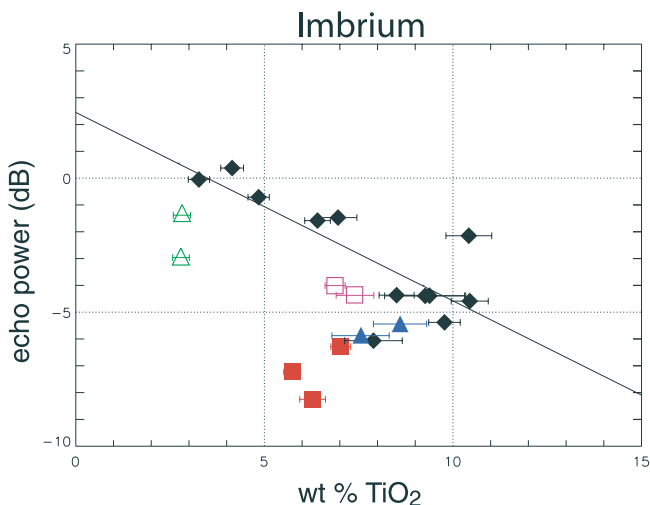


**Figure 12.** Plot of median echo power versus median weight%  $\text{TiO}_2$  for sample sites across Imbrium flows (boxes in Figure 11). Solid red squares correspond to sample sites for Delisle and Diophantus radar-dark haloes; solid blue triangles correspond to Euler; open green triangles correspond to Piazz-Smyth; and open magenta squares correspond to Timocharis. Horizontal error bars are standard deviations on median  $\text{TiO}_2$  values for sample sites.

ated with craters of different ages but with similar variations in chemistry should show similar slopes. For this reason, we can compare craters from all the mare basins to the Imbrium line shown in Figure 12. We selected at least four sample sites for each of the mare craters listed in Table 1; at least two inside each radar-dark halo and at least two representing the surrounding terrain. For each of these sites, we plotted median echo power versus median  $\text{TiO}_2$  content and compared the resulting plots to the trend established for the Imbrium samples. The slope of the Imbrium line represents the fraction of the offset in echo power between the haloes and the surrounding terrain that can be reasonably attributed to absorption of the radar energy by ilmenite. Thus, if the slope of the line drawn through the points represented by the crater haloes and background sites is steeper than the Imbrium line, we can conclude that the haloes are darker than they would be if they existed solely as a function of  $\text{TiO}_2$  content.

[28] Data corresponding to halo sample sites for five craters in Mare Imbrium are shown in Figure 12, plotted on the same set of axes as the Imbrium samples. The background terrain for these craters is represented by the Imbrium trend line. For these examples, the halo sites show lower echoes than predicted by the Imbrium line. This pattern persists for all of the mare craters in Table 1. For most of the craters, a clear separation on the order of 2–6 dB exists between the halo and background echoes, and the corresponding range of  $\text{TiO}_2$  values is generally at most 1–2%. These results indicate that (1) the previously noted inverse correlation between echo strength and  $\text{TiO}_2$  content for regional-scale flows in Imbrium holds using fully calibrated Clementine UV/VIS data, but (2) the offset in echo strength between radar-dark haloes and the background terrain for the mare craters listed in Table 1 is

greater than can be explained on the basis of variations in ilmenite abundance alone. Thus, though variations in  $\text{TiO}_2$  content may play a role for some mare craters, the magnitudes of these variations are insufficient to be solely responsible for the existence of radar-dark haloes associated with mare craters.

[29] We conclude that for the mare craters as well as the highland craters, the radar-dark haloes are likely evidence for a meters-thick layer of relatively fine material in the distal parts of the ejecta blanket associated with each crater (Figure 8). The fine layer responsible for the haloes is easier to observe, particularly for small craters, in mare areas because though the maria are generally darker at 70 cm than the highlands, they are more uniform in echo strength. As for the highland craters (section 4.1), 3.8-cm radar mosaics for the mare craters show no evidence for radar-dark haloes, suggesting that the fine layer is depleted in decimeter to meter-sized blocks. This interpretation is in agreement with the findings of *Schultz and Mendell* [1978] for Aristarchus; the current work has extended the analysis to the entire nearside of the Moon, and indicates that this distinctive block-poor ejecta characterizes many highland as well as mare craters. It should also be noted that workers such as *Schmitt et al.* [1967] have previously suggested that distal ejecta units associated with many nearside craters may be composed of fine-grained ejecta materials, consistent with our observations thus far. Similar to the highland craters, mare craters that show radar-dark haloes range from Late Imbrian to Copernican in age; older craters do not show dark haloes.

#### 4.5. Aristarchus and Herodotus A

[30] The region around Aristarchus crater shows a number of unique features and has been the subject of much study [e.g., *Zisk et al.*, 1977; *Guest and Spudis*, 1985; *Lucey et al.*, 1986]. Aside from the crater itself, the most notable feature is the Aristarchus Plateau, an upland region  $\sim 170$ – $220$  km in size, situated NW of Aristarchus crater. The surface of the Plateau appears dark in radar images and is apparently covered by an iron-rich pyroclastic mantling material [e.g., *Zisk et al.*, 1977; *Gaddis et al.*, 1985]. A number of volcanic features occupy the region, including Vallis Schröteri, the Moon's largest sinuous rille. Aristarchus Plateau, which appears red in optical true-color observations, is clearly visible as a low-return region in 70-cm radar images (Figure 13a), as a deep red region (consistent with its high-iron pyroclastic composition [*McEwen et al.*, 1994]) in the Clementine band-ratio map (Figure 13c) and as a topographically raised area in optical images (Figure 13d). Aside from the Plateau, a radar-dark halo is clearly visible in the OC-polarized radar image in Figure 13a; the halo shows an approximately smooth margin and constant width around the southern margin of the crater. This dark halo is analogous to the other haloes analyzed in this study; however, a set of approximately radial radar-dark spokes emanate from the halo to the south and southeast. The small crater Herodotus A, situated southwest of Aristarchus, also shows a well-defined, symmetric dark halo and two prominent spokes radiating to the west from the halo. These low-return spoke features are not observed at any of the other craters examined in this study. Comparison of these features with optical data shows

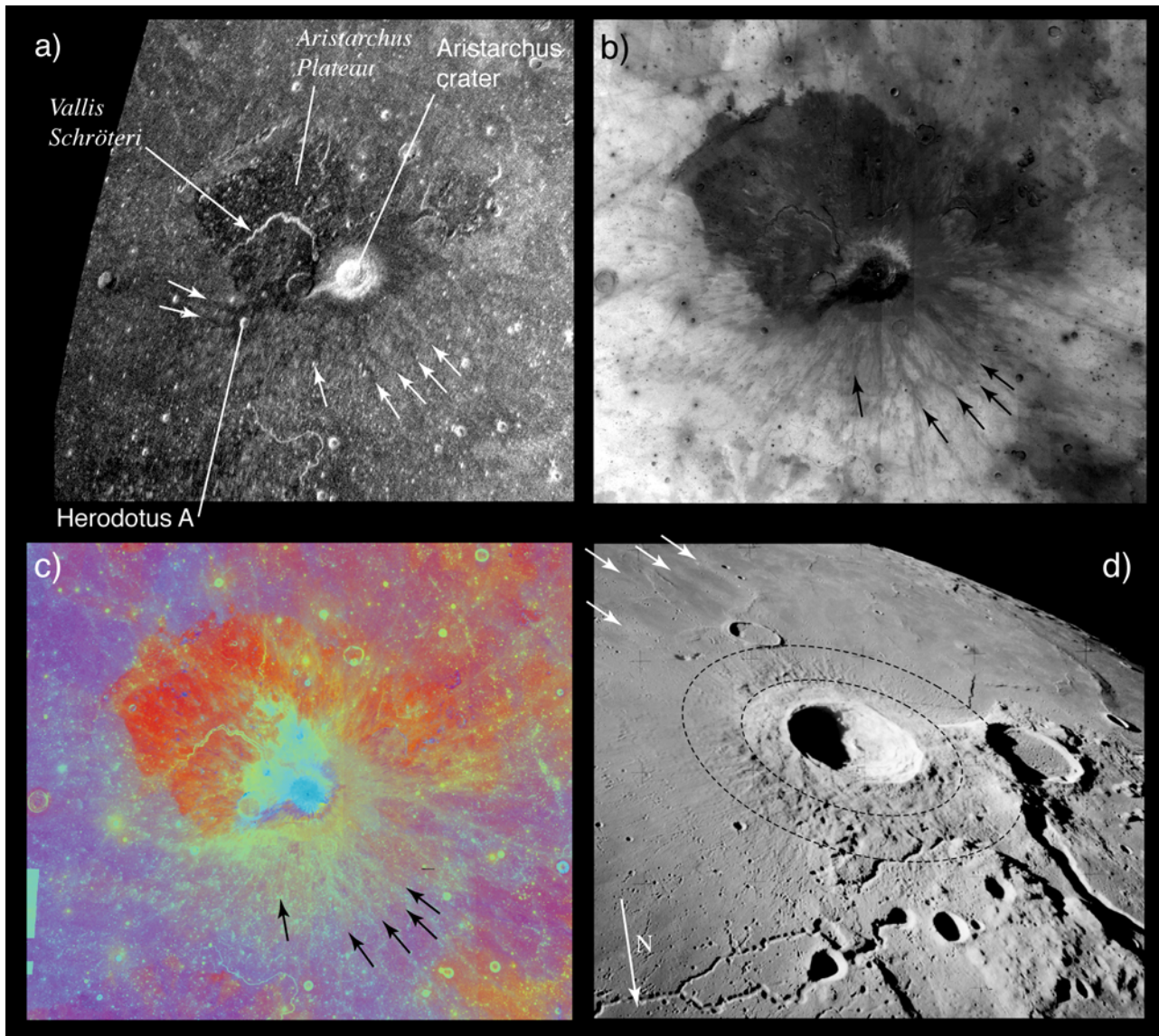


**Figure 13.** Remote-sensing images of the Aristarchus region; north is at top for all except Figure 13d. Diameter of Aristarchus: 40 km. (a) Seventy-centimeter OC radar image (13.0–34.5N, 35–60W); white arrows point to low-return spoke features. (b) Clementine TiO<sub>2</sub> map (15–35N, 35–60W); black arrows point to features with apparently low-TiO<sub>2</sub> content that correspond to low-return spokes in Figure 13a. (c) Clementine 3-color band ratio image of same area as Figure 13b; arrows are same as in Figure 13b. (d) Apollo 15 Hasselblad image A15-88-11980; inner dashed circle denotes extent of radar-bright ejecta; outer dashed circle indicates approximate boundary of radar-dark halo. Radial ejecta ridges are visible to the south of the crater; these features correspond with the radar-dark halo south of Aristarchus. Arrows denote radial high-albedo features distal to the ridged ejecta that correspond with the spokes in Figure 13a.

that the dark haloes and spoke features associated with Aristarchus show a correlation with radial ejecta material distal to the typical radial ridged ejecta (Figure 13d). These radial features also show a correlation with radial features in the TiO<sub>2</sub> map (Figure 13b), but with the opposite sense from that expected; rather than the predicted relationship between high TiO<sub>2</sub> content and low radar echo power, the haloes and spoke features seem to show low TiO<sub>2</sub> content instead. The Clementine band ratio image shows that the radial spoke material, apparently ejected from Aristarchus crater, does not have the same spectral characteristics as the iron-rich, dark

mantling material apparent on the Plateau. Instead, this material has a predominantly yellow-green color in the ratio image, suggesting a fresh mare basalt composition [McEwen *et al.*, 1994].

[31] At least two possible mechanisms for the formation of these spokes can be envisioned.

[32] 1. The material comprising these spokes is pyroclastic debris, ejected either from the Plateau region or from underlying layers by the Aristarchus impact. This is a reasonable hypothesis because the entire vicinity is well known as a site of pyroclastic activity on the Moon.

Because the spokes appear spectrally distinct from the Plateau pyroclastics, the spoke material could be derived from Plateau pyroclastics mixed with highland or mare material in the impact process, or from a distinct subsurface layer of pyroclastic material. If this spoke material is pyroclastic, the expression of the spokes in the radar images might be dominantly controlled by the chemistry of the ejected material. The composition of the spokes, however, may not be accurately reflected in the Clementine TiO<sub>2</sub> map, because the method used to calculate the TiO<sub>2</sub> abundance [Gillis *et al.*, 2003] is likely inappropriate for pyroclastic material, as pyroclastic glasses were not included in the algorithms used to derive the elemental compositions [e.g., Gaddis *et al.*, 2000]. In that case, the anomalous correlation between TiO<sub>2</sub> abundance and radar backscatter noted above may not exist. It is unknown, however, whether a sufficient volume of Plateau pyroclastics exists beneath the Procellarum basalts south of the crater to account for the spoke material.

[33] 2. In the second scenario, the dominant characteristic of the spoke material is that it is rock-poor and therefore attenuates the incident radar more effectively than the mare material between the spokes. This interpretation is supported by the work of Schultz and Mendell [1978], who suggested that small craters in the vicinity of Aristarchus, including Herodotus A, have a block-poor ejecta zone at 0.5 to 1 crater radii from the rim on the basis of Apollo ISR thermal data. If the spokes are indeed block-poor, and if they indeed have lower TiO<sub>2</sub> content (and thus lower loss tangent) than the surrounding mare, the resulting tendency toward stronger radar return is dominated by the block-poor nature of the ejecta. In this case, the spokes may exist uniquely in this location because Aristarchus is the youngest of the large mare craters, and thus the most fragile of the distal ejecta features have not yet been erased by the effects of bombardment.

[34] In either of these two scenarios, it seems clear that if compositional variations are responsible for the low returns exhibited by the halo and spoke features at Aristarchus and Herodotus A, these variations are not well represented in the Clementine-derived multispectral data presented here. Future acquisition of high-resolution dual-polarization (and possibly multiwavelength) radar data for this region will shed additional light on this issue.

## 5. Summary and Discussion

[35] The results of this study indicate that 70-cm radar-dark haloes are closely linked with impact crater ejecta properties. Loss tangent variations alone are insufficient to explain the presence of the haloes; instead, they more likely represent a mantling ejecta layer depleted in decimeter to meter-sized blocks. This fine layer attenuates incident microwave radiation, resulting in low SC returns and circular polarization ratios. Over time, the haloes brighten as the fine ejecta layer is eliminated by impact overturn and gardening processes, and possibly by production and/or brecciation of impact melt.

[36] This scenario is similar to the mechanism proposed for the production and evolution of radar-bright ejecta material by Thompson *et al.* [1981]. The authors of that study examined a large population of craters showing haloes

of material with bright returns at 3.8-cm corresponding to proximal ejecta with surface roughness and abundant blocks on the scale of 1–40 cm. These bright haloes are thought to disappear over time as rough surfaces are smoothed and as surface and subsurface rocks are fragmented by impacts of various sizes; the rate of this process is related to crater size. This evolution led Thompson *et al.* to suggest that a steady state population of craters with such bright haloes may exist, and that the presence and state of the bright haloes might be used for determining relative age relationships among craters. The population of craters with radar-dark haloes examined here is much smaller than the population of craters with radar-bright ejecta at 3.8-cm; nevertheless, the recognition of such radar-dark haloes may be useful for examining age relationships among craters. Our results show that craters older than Franklin and Petavius (of Early Imbrian age) no longer have radar-dark haloes associated with their ejecta materials; thus we can conclude that at least for some craters >50 km in diameter, a time period longer than the age of Franklin or Petavius is required for the halo materials to become completely homogenized with the surrounding regolith. This “halo maturation” time is likely size-dependent, with haloes associated with smaller craters disappearing faster than those associated with large craters like Petavius. The number of craters with radar-dark haloes is too small to support a size-frequency analysis like that performed by Thompson *et al.* [1981]; however, with continued acquisition of high-resolution, dual-polarization observations at 70-cm, it will be possible to conduct a more exhaustive search for small craters with radar-dark haloes. Because the degradation of radar-bright and radar-dark haloes occurs by essentially the same physical process, we may be able (with a sufficiently large population of dark-haloed craters) to relate the “maturation rates” of radar-dark haloes and radar-bright haloes in a way that would lead to an understanding of the scale- and depth-dependent rates of modification of regolith materials by lunar surface processes.

[37] A comprehensive, dual-polarization 70-cm radar survey of the entire lunar nearside will provide a wealth of additional information regarding the surface and subsurface physical properties of the regolith. Furthermore, analysis of a complete database of craters with radar-dark and radar-bright haloes at multiple radar wavelengths could dramatically increase our understanding of the processes of ejecta degradation. Such a study would bear on other related work. For example, McEwen *et al.* [1993] used Galileo multispectral data in conjunction with crater counts derived from Lunar Orbiter images to make relative age determinations for a number of farside craters, and to propose revisions to accepted age classifications for certain nearside craters, including Bullialdus, Diophantus, and Hausen, which we address in our study. More recently, Hawke *et al.* [2004] used multiwavelength radar observations in conjunction with Clementine multispectral data to investigate the nature of lunar crater rays, and proposed that the presence of rays alone is insufficient to define the population of Copernican-aged craters. A detailed hemispheric characterization of ejecta degradation processes as reflected in multiwavelength radar observations would complement these types of analyses, and together could lead to a refinement of the lunar geologic timescale.

[38] **Acknowledgments.** This work was supported in part by grants from the NASA Planetary Geology and Geophysics Program. Arecibo Observatory is operated by Cornell University under contract from the NSF. The Greenbank Telescope is operated by the National Radio Astronomy Observatory. The authors thank J. Chandler for producing the lunar ephemeris files and the staff of Arecibo and the GBT for observing assistance. We also thank Peter Schultz and an anonymous reviewer for thoughtful comments that improved the quality of the manuscript.

## References

- Campbell, B. A. (2002), *Radar Remote Sensing of Planetary Surfaces*, Cambridge Univ. Press, New York.
- Campbell, B. A., B. R. Hawke, and T. W. Thompson (1997), Regolith composition and structure in the lunar maria: Results of long-wavelength radar studies, *J. Geophys. Res.*, 102(E8), 19,307–19,320.
- Carr, M. H. (1966), Geologic map of the Serenitatis Quadrangle of the Moon, *U.S. Geol. Surv. Misc. Geol. Invest., Map I-489(LAC-42)*.
- Carrier, W. D., G. R. Olhoeft, and W. Mendell (1991), Physical properties of the lunar surface, in *Lunar Sourcebook: A User's Guide to the Moon*, edited by G. Heiken et al., pp. 475–594, Cambridge Univ. Press, New York.
- Casella, C. J., and A. B. Binder (1972), Geologic map of the Cleomedes Quadrangle of the Moon, *U.S. Geol. Surv. Misc. Geol. Invest., Map I-707(LAC-44)*.
- Gaddis, L. R., C. M. Pieters, and B. R. Hawke (1985), Remote sensing of lunar pyroclastic mantling deposits, *Icarus*, 61, 461–489.
- Gaddis, L. R., B. R. Hawke, M. R. Robinson, and C. Coombs (2000), Compositional analyses of small pyroclastic deposits using Clementine multispectral data, *J. Geophys. Res.*, 105(E2), 4245–4262.
- Gillis, J. J., B. L. Jolliff, and R. C. Elphic (2003), A revised algorithm for calculating TiO<sub>2</sub> from Clementine UVVIS data: A synthesis of rock, soil, and remotely sensed TiO<sub>2</sub> concentrations, *J. Geophys. Res.*, 108(E2), 5009, doi:10.1029/2001JE001515.
- Guest, J. E., and P. D. Spudis (1985), The Aristarchus impact event and the effects of target material, *Geol. Mag.*, 122(4), 317–327.
- Hawke, B. R., and J. F. Bell (1981), Remote sensing studies of lunar dark-halo impact craters: Preliminary results and implications for early volcanism (abstract), *Proc. Lunar Planet. Sci. Conf. 12B*, 665–678.
- Hawke, B. R., D. T. Blewett, P. G. Lucey, G. A. Smith, J. F. Bell III, B. A. Campbell, and M. S. Robinson (2004), The origin of Lunar Crater Rays, *Icarus*, 170, 1–16.
- Johnson, J. R., S. M. Larson, and R. B. Singer (1991), Remote sensing of potential lunar resources: I. Near side compositional properties, *J. Geophys. Res.*, 96, 18,861–18,882.
- Lucchitta, B. (1972), Geologic map of the Aristoteles region of the Moon, *U.S. Geol. Surv. Misc. Invest., Map I-725(LAC-13)*.
- Lucey, P. G., B. R. Hawke, C. M. Pieters, J. W. Head, and T. B. McCord (1986), A compositional study of the Aristarchus region of the Moon using near-infrared reflectance spectroscopy, *Proc. Lunar Planet. Sci. Conf. 16th*, Part 2, *J. Geophys. Res.*, 91, suppl., D344–D354.
- Lucey, P. G., G. J. Taylor, and E. Malaret (1995), Abundance and distribution of iron on the Moon, *Science*, 268, 1150–1153.
- Lucey, P. G., D. T. Blewett, J. L. Johnson, G. J. Taylor, and B. R. Hawke (1996), Lunar titanium content from UV-VIS measurements (abstract), *Lunar Planet. Sci., XXVII*, 781–782.
- Lucey, P. G., D. T. Blewett, and B. L. Jolliff (2000a), Lunar iron and titanium abundance algorithms based on final processing Clementine UVVIS images, *J. Geophys. Res.*, 105(E8), 20,297–20,305.
- Lucey, P. G., D. T. Blewett, G. J. Taylor, and B. R. Hawke (2000b), Imaging of lunar surface maturity, *J. Geophys. Res.*, 105(E8), 20,377–20,386.
- McCauley, J. F. (1967), Geologic map of the Hevelius region of the Moon, *U.S. Geol. Surv. Misc. Geol. Invest., Map I-491(LAC-56)*.
- McEwen, A. S., L. R. Gaddis, G. Neukum, H. Hoffman, C. M. Pieters, and J. W. Head (1993), Galileo observations of post-Imbrium lunar craters during the first Earth-Moon flyby, *J. Geophys. Res.*, 98(E9), 17,207–17,231.
- McEwen, A. S., M. S. Robinson, E. M. Eliason, P. G. Lucey, T. C. Duxbury, and P. D. Spudis (1994), Clementine observations of the Aristarchus region of the Moon, *Science*, 266, 1858–1862.
- Melosh, H. J. (1996), *Impact Cratering: A Geologic Process*, Oxford Monogr. Geol. Geophys., vol. 11, Oxford Univ. Press, New York.
- Moore, H. J. (1967), Geologic map of the Seleucus region of the Moon, *U.S. Geol. Surv. Misc. Geol. Invest., Map I-527(LAC-38)*.
- Oberbeck, V. R. (1975), The role of ballistic erosion and sedimentation in lunar stratigraphy, *Rev. Geophys.*, 13, 337–362.
- Olson, A. B., and D. E. Wilhelms (1974), Geologic map of the Undarum Quadrangle of the Moon, *U.S. Geol. Surv. Misc. Geol. Invest., Map I-837(LAC-62)*.
- Page, N. J. (1970), Geologic map of the Cassini Quadrangle of the Moon, *U.S. Geol. Surv. Misc. Geol. Invest., Map I-666(LAC-25)*.
- Saunders, R. S., and D. E. Wilhelms (1974), Geologic map of the Wilhelm Quadrangle of the Moon, *U.S. Geol. Surv. Misc. Geol. Invest., Map I-824(LAC-III)*.
- Schaber, G. G., T. W. Thompson, and S. H. Zisk (1975), Lava flows in Mare Imbrium: An evaluation of anomalously low Earth-based radar reflectivity, *Moon*, 13, 395–423.
- Schmitt, H. H., N. J. Trask, and E. M. Shoemaker (1967), Geologic map of the Copernicus Quadrangle of the Moon, *U.S. Geol. Surv. Misc. Geol. Invest., Map I-515(LAC-58)*.
- Schultz, P. H. (1976), Floor-fractured lunar craters, *Moon*, 15, 241–273.
- Schultz, P. H., and D. E. Gault (1985), Clustered impacts: Experiments and implications, *J. Geophys. Res.*, 90(B5), 3701–3732.
- Schultz, P. H., and W. Mendell (1978), Orbital infrared observations of lunar craters and possible implications for impact ejecta emplacement, *Proc. Lunar Planet. Sci. Conf. 9th*, 2857–2883.
- Scott, D. H., J. F. McCauley, and M. N. West (1977), Geologic map of the west side of the Moon, *U.S. Geol. Surv. Misc. Invest. Ser., Map I-1034*.
- Stacy, N. J. S. (1993), High-resolution synthetic aperture radar observations of the Moon, Ph.D. thesis, 210 pp., Cornell Univ. and Natl. Astron. and Ionosphere Cent., Ithaca, N. Y.
- Thompson, T. W. (1974), Atlas of lunar radar maps at 70-cm wavelength, *Moon*, 10, 51–85.
- Thompson, T. W. (1987), High resolution lunar radar map at 70-cm wavelength, *Earth Moon Planets*, 37, 59–70.
- Thompson, T. W., J. B. Pollack, M. H. Campbell, and B. T. O'Leary (1970), Radar maps of the Moon at 70-cm wavelength and their interpretation, *Radio Sci.*, 5(2), 253–262.
- Thompson, T. W., T. V. Johnson, D. L. Matson, R. S. Saunders, R. W. Shorthill, S. H. Zisk, H. J. Moore, and G. G. Schaber (1978), Unusual remote sensing signatures of Montes Jura and Crater Plato (abstract), *Proc. Lunar Planet. Sci. Conf. 9th*, 1164–1165.
- Thompson, T. W., S. H. Zisk, R. W. Shorthill, P. H. Schultz, and J. A. Cutts (1981), Lunar craters with radar bright ejecta, *Icarus*, 46, 201–225.
- Turcotte, D. L. (1992), *Fractals and Chaos in Geology and Geophysics*, Cambridge Univ. Press, New York.
- Ulaby, F. T., R. K. Moore, and A. K. Fung (1982), *Microwave Remote Sensing*, Addison-Wesley, Boston, Mass.
- Whitford-Stark, J. L., and J. W. Head III (1980), Stratigraphy of Oceanus Procellarum basalts: Sources and styles of emplacement, *J. Geophys. Res.*, 85(B11), 6579–6609.
- Wilhelms, D. E. (1980), Stratigraphy of part of the lunar nearside, *U.S. Geol. Surv. Prof. Pap.*, 1046-A.
- Wilhelms, D. E. (1987), The geologic history of the Moon, *U.S. Geol. Surv. Prof. Pap.*, 1348.
- Wilhelms, D. E., K. A. Howard, and H. G. Wilshire (1979), Geologic map of the south side of the Moon, *U.S. Geol. Surv. Misc. Invest. Ser., I-1162*.
- Wilshire, H. G. (1973), Geologic map of the Byrgius Quadrangle of the Moon, *U.S. Geol. Surv. Misc. Geol. Invest., I-755(LAC-92)*.
- Zisk, S. H., G. H. Pettengill, and G. W. Catuna (1974), High-resolution radar maps of the lunar surface at 3.8-cm wavelength, *Moon*, 10, 17–50.
- Zisk, S. H., C. A. Hodges, H. J. Moore, R. W. Shorthill, T. W. Thompson, E. A. Whittaker, and D. E. Wilhelms (1977), The Aristarchus-Harbinger region of the Moon: Surface geology and history from recent remote-sensing observations, *Moon*, 17, 59–99.

B. A. Campbell, R. R. Ghent, and D. W. Leverington, Center for Earth and Planetary Studies, Smithsonian Institution, MRC 315, P.O. Box 37012, Washington, DC 20013-7012, USA. (ghentr@nasm.si.edu)

D. B. Campbell, Department of Astronomy, Cornell University, Ithaca, NY 14853, USA.

B. R. Hawke, Hawaii Institute of Geophysics and Planetology, School of Ocean and Earth Science and Technology, Honolulu, HI 96822, USA.